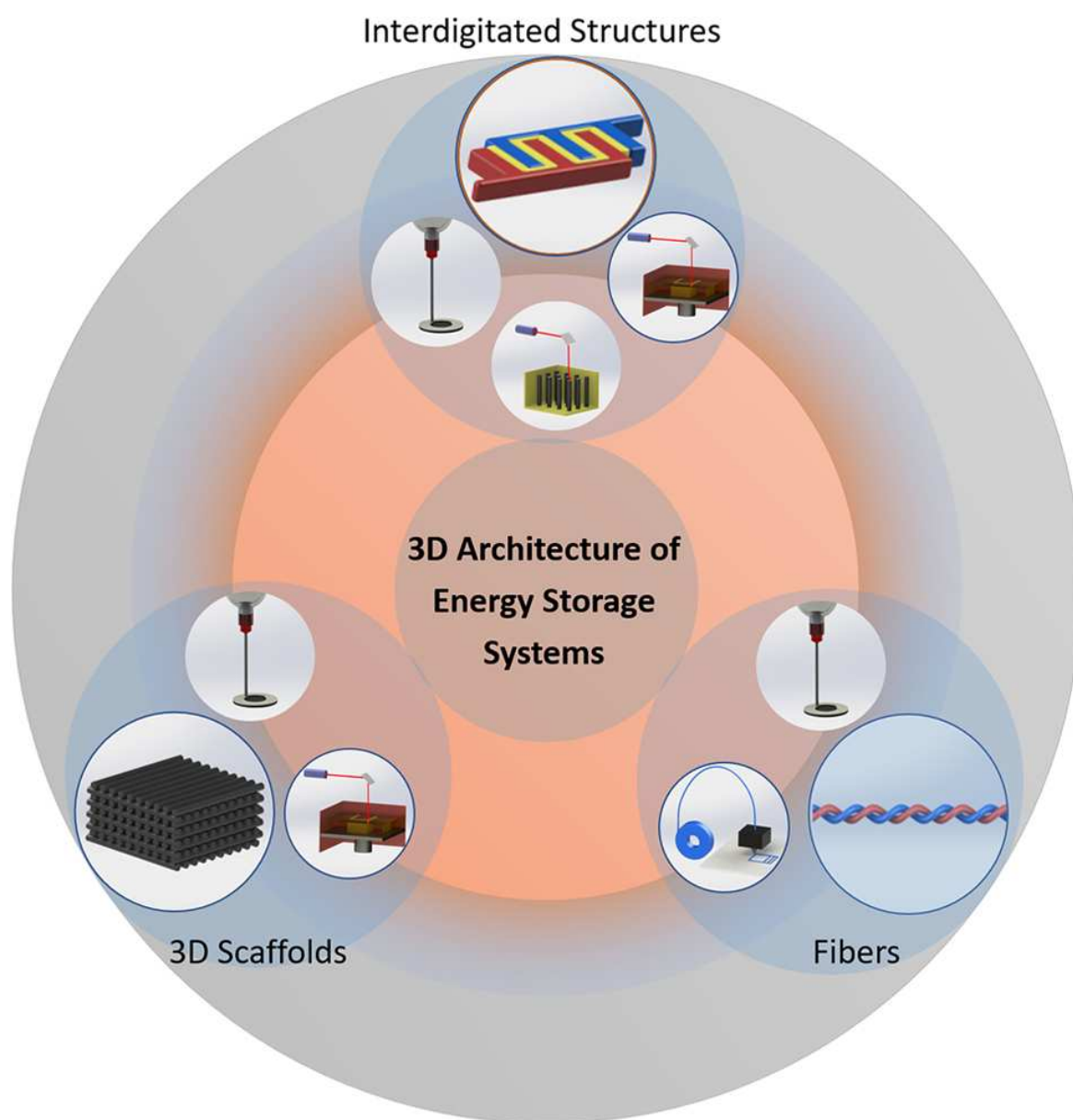


3D Printing of Electrochemical Energy Storage Devices: A Review of Printing Techniques and Electrode/Electrolyte Architectures

Meng Cheng,^[a] Ramasubramonian Deivanayagam,^[a] and Reza Shahbazian-Yassar^{*[a]}



Recently, the fabrication of electrochemical energy storage (EES) devices via three-dimensional (3D) printing has drawn considerable interest due to the enhanced electrochemical performances that arise from well-designed EES device architectures as compared to the conventionally fabricated ones. This work summarizes the developments in electrochemical devices fabricated by 3D printing techniques. We have categorized this review based on the architectural design of 3D printed EES devices: interdigitated structures, 3D scaffolds, and fibers. The printing techniques, processes, printing materials, advantages, and disadvantages of 3D printed architectures are

systematically discussed in this review. Enhanced power density and energy density values were obtained using interdigitated structures and 3D scaffolds, in comparison with the conventional planar structure. The reasons for better electrochemical performances can be attributed to the presence of higher loading active materials, larger footprint area, and shorter ion transport route. The 3D printing techniques have also enabled the EES devices to be fabricated into lightweight, flexible fibers, and to be integrated into wearable electronics. At the end, the challenges and outlooks on the fabrication of 3D structured EES devices are outlined.

1. Introduction

Electrochemical energy storage (EES) devices, such as batteries, supercapacitors and their hybrid devices, have been considered as promising energy storage systems, due to their high power density, energy density, long cycle life, and their ability to supply clean energy.^[1–4] Generally, an integrated EES system is composed of the following components: two electrodes, current collectors, electrolytes and a membrane.^[5] The materials of each of these components, their structures, and the fabrication methods, are considered as the most important factors affecting the performances of EES devices. From the materials perspective, although the EES devices have undergone extensive developments over the last few decades, modifications in the manufacturing techniques of EES devices has only been rarely explored. This is in part due to the existing limitations of conventional fabrication methods. Several manufacturing techniques, such as sputtering,^[6] pulsed-laser deposition,^[7–9] photolithography,^[10] and epitaxial growth,^[11] can already meet the geometry requirements of EES devices to a certain degree. However, in these techniques, the required working environments, the generated material wastes, the complicated steps involved, and variations made in the geometric molds could result in the increase in cost of prototype developments. Additionally, these technologies may require the use of toxic materials in components such as lubricants and coolants, which make their adoption less appealing.^[12]

Additive manufacturing, also known as 3D-printing, has gained significant attention as an advanced manufacturing technique for fabricating complex freeform geometries at a relatively low cost.^[13] Additive manufacturing, a manufacturing technique in which three-dimensional objects are created through an additive process, is known to be more flexible and cost-effective than the traditionally-used subtractive methods in which materials are successively removed from a bulk material (e.g. milling).^[14–15] Since 3D printing can be extended to almost all types of materials such as metals,^[16–17] ceramics,^[18]

polymers,^[19] composites,^[20–21] and biomaterials,^[22–23] this technique has currently been applied to a wide range of applications, including electronics,^[24–25] biotechnology,^[26–27] and construction.^[28–29] Recently, 3D printing of EES devices with a variety of geometries has been explored and developed in order to improve their energy density, power density and mechanical properties.^[30–33]

The major advantage of additive manufacturing is that the architecture of EES devices can be highly controlled, which is in sharp contrast to the conventional manufacturing techniques. Customized EES devices down to micro-size can be achieved by 3D printing.^[34] With the improvements brought about in the design of architectures, the 3D printed EES devices have the following superiorities (Figure 1):

- (1) Enhanced specific capacity/capacitance, energy density, power density of EES devices are attained through 3D printing. For the conventional EES devices with sandwich structure, one of the common strategies to improve the energy density is to increase the thickness of electrodes with more mass loading of active materials.^[35–36] However,

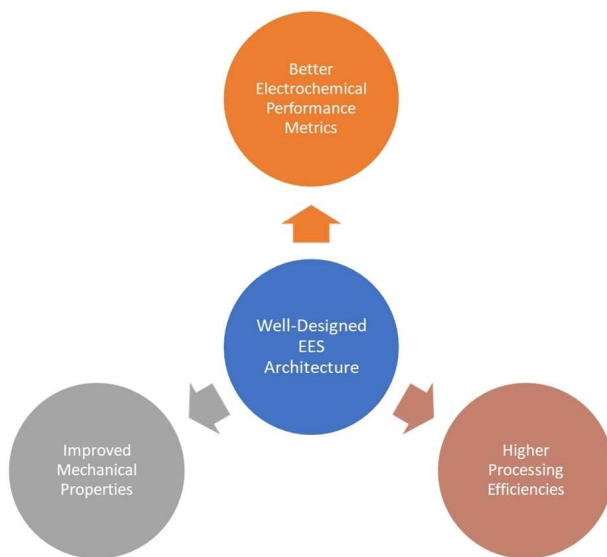


Figure 1. Schematic summary: the advantages of 3D printing of EES devices with well-designed architecture in better electrochemical performance, higher processing efficiencies, and improved mechanical properties.

[a] M. Cheng, R. Deivanayagam, Prof. R. Shahbazian-Yassar
Department of Mechanical and Industrial Engineering,
University of Illinois at Chicago
E-mail: rsyassar@uic.edu

An invited contribution to a Special Collection dedicated to the Symposium on Batteries and Supercapacitors at the E-MRS Spring Meeting 2019

increasing the electrode thickness could lead to longer ion diffusion paths which in turn results in higher resistance, and lower power densities. This drawback can be addressed by 3D printing of EES devices with well-designed structures, for instance, interdigitated structures. For EES devices with interdigitated structures, the width of electrodes and electrolytes can be highly controlled during the 3D printing process. Hence, the energy density of EES devices can be enhanced by increasing the height of electrodes with more mass loading of active materials. Moreover, with 3D printing, the enhancement of energy density of EES devices does not need to be at the expense of sacrificing their power density.^[35,37]

- (2) Improvements in mechanical properties, especially high flexibility, is an emerging direction pursued by the manufacturers of next generation EES devices for wearable electronics. Compared with 2D and 3D flexible EES devices, 1D fiber-shaped EES devices present higher feasibility to be woven into flexible textiles for wearable applications.^[33,38–40] Among the various fabrication strategies, incorporation of twisted fiber-shaped EES devices directly into the textiles for wearable applications is a low-cost and efficient method.
- (3) Due to the versatility, wide-scale flexibility and material selection of the technique, 3D printing of EES devices provides a chance to integrate the fabrication of the whole EES device and all accompanying electronics in a single manufacturing step, which is far more cost-effective than separately fabricating the components and assembling them.^[41–42]

Several breakthrough reports on 3D printed EES devices with complex architectures have been published over the past few years.^[43–48] In addition, the feasibility of 3D printed EES devices in wearable devices has also been explored.^[33,49] Although a few reviews on 3D printed EES devices exist in the literature, prior reviews have focused on the aspects of the

printing technology and printing materials, with only a limited discussion on the types of architectures that can be produced.^[3,50–51] However, this review sets out to detail the types of architectures that have been developed over the years, and their impact on the electrochemical performances and mechanical properties of the EES devices, along with the advantages and disadvantages of the production techniques involved. In contrast to other existing reviews,^[3,50,52–53] we have placed more emphasis on classification of devices based on the obtained 3D structures, and on the comparison of the advantages, disadvantages, and the performance metrics of the devices themselves. The state-of-the-art research developments are covered in two different sections: (i) the various 3D printing techniques currently being implemented into the fabrication of EES devices, and (ii) the main characteristics of each of the 3D printed architectures. Then, a comparison is made between various 3D architectures. Furthermore, the review outlines the fundamental difficulties of using 3D printing technique as a manufacturing method of EES devices, and concludes with listing the possible innovations for developing 3D printed EES devices.

2. 3D Printing Technology

According to ASTM International (formerly known as American Society for Testing and Materials), 3D printing can be categorized into seven main types (Figure 2):^[54] (1) sheet lamination (e.g. laminated object manufacturing, and ultrasonic consolidation), (2) binder jetting, (3) directed energy deposition (e.g. electron beam freeform fabrication), (4) material extrusion (e.g. direct writing and fused deposition modeling), (5) material jetting, (6) vat photopolymerization (e.g. stereolithography), and (7) powder bed fusion (e.g. Electron beam melting and selective laser sintering). In recent years, various state-of-art 3D printing methods, such as direct ink writing, fused deposition



Meng Cheng is currently a Ph.D. candidate in the department of Mechanical and Industrial Engineering at the University of Illinois at Chicago working under the supervision of Prof. Reza Shahbazian-Yassar. He obtained his M.S. in Advanced Materials Science from University of Liverpool in 2012 and his B.E. in Mechanical System and Design Engineering from University of Liverpool in 2011. His research interests are all-solid-state Li-ion batteries and all-3D-printing of electrochemical energy storage devices.



Ramasubramonian Deivanayagam is currently a Ph.D. candidate at the University of Illinois at Chicago working under the supervision of Prof. Reza Shahbazian-Yassar. He received his dual degree of B.S. and M.S. in Physics in 2015 from Indian Institute of Science Education and Research (IISER) Thiruvananthapuram, where he carried out his Master's thesis research under the guidance of Prof. M. M. Shajumon.



His research interests include developing materials for all-solid-state rechargeable lithium-ion and magnesium batteries.

Reza Shahbazian-Yassar is currently a professor of Mechanical and Industrial Engineering at the University of Illinois at Chicago. Prior to this position, he was a Henes Chair Associate Professor of Nanotechnology at Michigan Technological University. He received his PhD in Materials Science from Washington State University in Pullman, WA, in 2005. His research is mainly focused on (1) advanced manufacturing for batteries; (2) *in situ* TEM of functional nanomaterials; and (3) material design for safe and high energy density batteries.

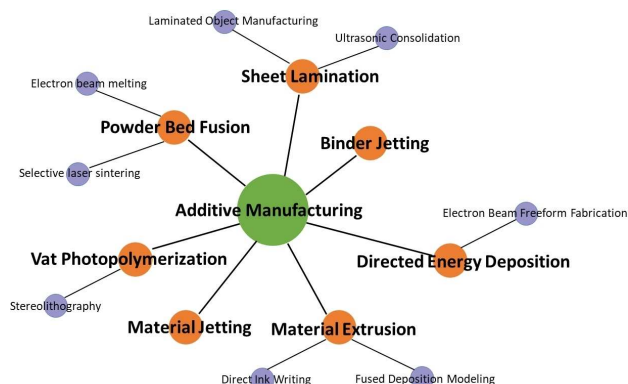


Figure 2. Network showing the various types of additive manufacturing working principles (shown in orange). Each of the working principles can be further categorized by either the type of feed material used for printing or their energy source (purple circles).

modeling, stereolithography, selective laser sintering, ink-jet printing and binder jetting have been used to fabricate EES devices. Among these, the most common techniques adopted for fabrication of 3D architectures are direct ink writing, fused deposition modeling, stereolithography, and selective laser sintering. On the other hand, the reported architectures of EES devices printed using binder jetting or inkjet printing consisted of 2D plane structures.^[55–58] Therefore, in the following section, we restrict our discussion to DIW, SLA, FDM, and SLS 3D printing techniques in order to emphasize on the unique 3D structures made possible by these technologies.

2.1. Direct Ink Writing (DIW)

Direct ink writing is a fabrication method used to create freeform structures by dispensing ink through a nozzle, which is controlled by a computer (Figure 3A). After printing, the printed structure is cured through either liquid evaporation, gelation, a solvent driven reaction, or thermal energy.^[59] To print EES devices architectures with a high-resolution, the ink design is a crucial factor. Basically, a shear-thinning behavior is desirable for printable inks.^[59–60] Shear-thinning behavior refers to the decreasing viscosity of fluids with increasing shear rate. With this behavior, the viscosity of the ink is reduced under pneumatic or mechanical force, and therefore the fluid can flow smoothly through the nozzle of printer. To optimize the rheology of inks and thereby enhance their electrochemical and mechanical properties, the addition of nanosized materials as fillers has been reported as a promising method. Two-dimensional layered nanomaterials such as graphene oxide (GO) have been widely used to tune the rheological properties of inks.^[47–48,61–62] Compared with polymer-based and cellulose-based viscosifiers,^[34,63] GO exhibits higher electrical conductivity after it is converted to reduced graphene oxide (r-GO) by annealing the printed electrodes.^[61] Addition of ceramic nanoparticles, such as TiO₂ and Al₂O₃,^[64–65] as fillers has also been reported as a promising strategy to obtain desired rheological

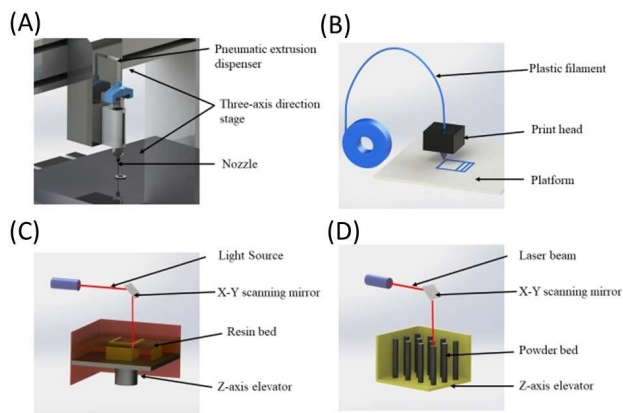


Figure 3. Common techniques used in 3D-printing of materials: A. Direct ink writing (DIW): freeform structures by depositing ink onto a platform.^[65] Reproduced with permission from Ref. [65]. Copyright 2018 Wiley-VCH. B. Fused deposition modeling (FDM): filaments (usually a spool of a polymeric material) are extruded through a heated nozzle and printed onto a platform in a similar fashion as direct ink writing. C. Stereolithography (SLA): a bath of a liquid photo-curable resin/polymer is subjected to a light source where the light source polymerizes the resin, forming a solid structure. D. Selective laser sintering (SLS): a laser is applied over a powdered material which the heat from the laser sinters the powder and thus forming a solid material.

properties and improved ionic conductivities for the electrolyte inks.

High performing ink formulations exhibit the desired rheology for printing,^[59,66–67] and the ability to be printed to feature sizes as low as 200 µm.^[68–69] The main advantages of using DIW for 3D printing of EES is the possibility of broad raw material selection, wide print feature size, and the potential to produce integrated smart packages since the technique can be used to directly print on any surface.

2.2. Fused Deposition Modeling (FDM)

Fused deposition modeling, shown in Figure 3B, is one of the most popular methods used in both industry and academia. Unlike the rigid requirements about rheological properties of inks for DIW, there are fewer requirements of materials for FDM, which are based on thermoplastic polymers. The mechanism of fused deposition modeling is similar to that of direct ink writing where a solid-state filament is extruded through a heated nozzle.^[70] During the printing process, the filament is melted and deposited onto a substrate, which upon natural cooling, turns back into a solid. Despite its popularity, FDM has rarely been used in 3D printing of EES devices due to the relatively low electrical conductivity of plastic filaments.^[71] Indeed, there are commercial graphene PLA filaments that have superior conductivity and improved mechanical properties. However, the low concentration of graphene (8–10 wt%) does not result in a significant improvement in the electrical conductivity of the filaments.^[72]

Recently, reports indicated that the optimization of the loading of active materials and conductive materials is a successful way to overcome the electrical conductivity

barrier.^[73–74] For instance, Maurel *et al.* demonstrated electrode filaments with highly loaded active and conductive materials with the configuration, PLA/graphite/carbon-black, whose weight ratio of 45.9/49.2/4.9.^[73] The electrode disc was fabricated by feeding the filament into an FDM 3D printer, and a reversible capacity of 200 mAh g⁻¹ at current density of 18.6 mA g⁻¹ was obtained for a cell with the printed electrode disc. With its ability to manufacture safely in an office-friendly environment,^[75] FDM provides an opportunity to commercialize 3D printing of EES devices.

2.3. Stereolithography (SLA)

Stereolithography is another 3D-printing technology that is rapidly gaining popularity amongst the 3D printing community.^[76] Stereolithography involves using a light source to polymerize a photocurable resin, resulting in the formation of a solid polymeric layer (Figure 3C).^[77] A moveable resin platform contained in a vat of the photo-curable resin provides support for each layer during the polymerization step. After a complete layer has been formed, the platform is repositioned, and hence a new layer can be printed. The movement of the platform during repositioning depends on the type of stereolithography. In top-down SLA, the platform is lowered for each consecutive layer, whereas in bottom-up SLA, it is raised.^[77] After the platform has been repositioned, a blade is used to push more photo-curable resin over the preceding layer before the next polymerization step. Since SLA is capable of printing extremely complex structures, this technique has a high potential for use in the 3D printing of EES devices.^[45,78]

Compared with 3D extrusion-based printing technologies (e.g. DIW, FDM, etc.), truly arbitrary design can be realized via SLA because this technology is not limited by the toolpath or serial extrusion.^[79] Therefore, 3D geometries with a variety of hollow carved features at macroscale can be achieved using SLA technology. Interestingly, a graphene-based photocurable resin has been recently synthesized to print high surface macroscale 3D architecture.^[79–80] The graphene with printed complexity structure shows an enhanced mechanical property and electrical conductivity which provide inspiration for the application in EES devices.

2.4. Selective Laser Sintering (SLS)

Selective laser sintering is an advanced additive manufacturing technique in which a laser is used to fuse powder materials into a solid, three-dimensional object. During the printing process, dense powder materials are placed on moveable platform. It is worth mentioning that the powder materials could be metal, polymer, and ceramic, which is more flexible in applications compared to other 3D printing techniques.^[81] In this process, a layer of powders is fused along with an established route by high-energy source either a CO₂ or Nd: YAG laser beam (Figure 3D).^[81] Once the first layer solidifies, the platform is lowered to give way for the second layer of

powders. After all the powder layers are fused and rest of unfused powders are removed, the desired printing structure is obtained. The major advantage of SLS 3D printing of EES devices is that the metal components such as current collector can also be printed using the same technique. Although a wide variety of materials could be directly used for SLS, the high cost of equipment and difficulty in operation are the main obstacles in adopting SLS in 3D printing of EES devices.

Unconstrained by the limitations of printable inks and UV-curable resins, the SLS technique enables highly efficient 3D printing of carbon-based composite electrodes.^[82] Although organic binder materials are still required for 3D printing carbon-based electrodes, the binder can be incorporated into the carbon structure during the laser processing, which further increases improved physical properties and electrical conductivity.^[82–83] Bauer *et al.* presented carbon nano-lattices structure with high specific strength which was transformed from 3D-printed polymeric micro-lattices after pyrolysis.^[83] The novel approach is quite effective for high-resolution 3D printing of carbon nano-lattices structure which can be adopted for manufacturing EES devices.

Factors such as accuracy, printing speed, range of candidate materials, and cost play an important role in determining the efficacy of 3D printing techniques. Table 1 lists the comparison of DIW, SLA, FDM and SLS. Broad material selection, fast printing speed, high resolution and low cost are the main reasons that led to the increasing popularity of DIW over the last few years.^[34,67] Nevertheless, there are challenges in the ink design that need to be addressed.^[59] The major advantages of FDM are low cost, high printing speed and large size capabilities.^[75,84] However, in comparison with DIW, SLA, and SLS techniques, the accuracy and surface finish of FDM is relatively low due to the limited flexibility of nozzle size.^[75,85] Truly arbitrary 3D architectures with high resolution and good surface finish can be achieved by SLA, but the printing materials are restricted to photopolymer-based materials.^[79] Additionally, the efficiency of SLA is relatively low.^[86–87] The widest possible range of materials can be printed by SLA in high resolution. However, the poor reusability of unsintered powder generates a high cost of the printing method.^[88]

3. 3D Architecture of EES Systems

Although the use of printing techniques in industry and research has exploded over the recent years, it has just started to making headway into the EES device community. Figure 4 shows a summary of the most recent innovations in the architecture of 3D printing of EES devices. There are three

Table 1. Comparison of DIW, SLA, FDM, and SLS.

| | Accuracy | Printing Speed | Materials | Cost |
|-----|-----------|----------------|--------------------------|-----------|
| DIW | High | High | Polymer, gel, ceramic | Low |
| FDM | Low | High | Photocurable materials | Low |
| SLA | Very high | Low | Thermoplastic polymer | High |
| SLS | High | High | Polymer, ceramic, metals | Very High |

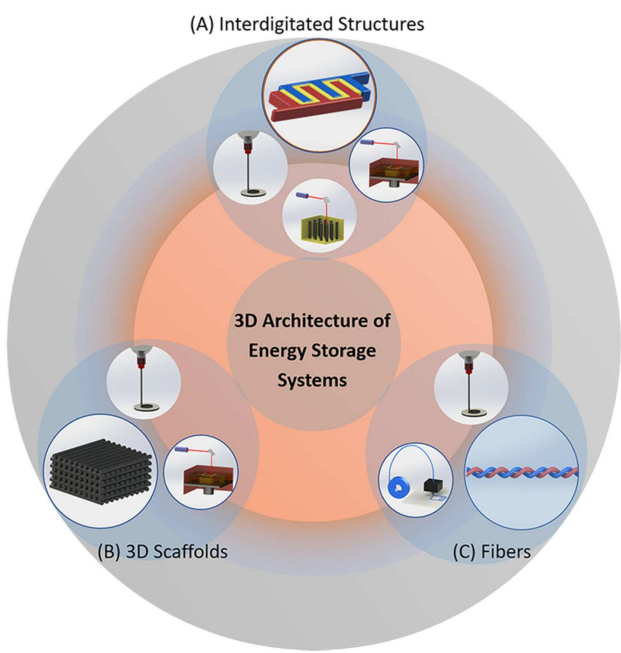


Figure 4. Additive manufacturing techniques used in the fabrication of 3D Architecture of EES components. In the fabrication of 3D architecture of EES components, four additive manufacturing techniques have been reported. **A.** Interdigitated structures has been produced by DIW, SLA and SLS. **B.** Complex 3D scaffolds can be completed by high resolution additive manufacturing techniques such as DIW and SLA. **C.** Fiber electrodes can be achieved by DIW, and the filaments of FDM could be considered as fibers electrodes.

major 3D architectures reported so far, namely interdigitated structures (Figure 4A), 3D scaffolds (Figure 4B) and fibers (Figure 4C). Among them, EES devices with interdigitated structures and 3D scaffolds are designed for high electrochemical performances requirements applications. The fibers are mainly utilized in flexible and wearable devices.

3.1. Interdigitated Structures

The interdigitated structure of EES devices features two interdigitated electrodes isolated by a narrow gap. The width of the gap and thickness of electrodes significantly influence the performances of the EES devices. With the high controllability of 3D printing, the width of the gap and thickness of electrolyte can also be adjusted. Compared with the EES devices with traditional sandwich structure, the hierarchical 3D interdigitated electrodes provide large surface area for ion diffusion and offer a pathway for fast electron transfer, resulting in increased efficiency and performance of EES devices.^[89]

One of the first works in fabricating a 3D-printed battery was demonstrated with an interdigitated battery design by Lewis and co-workers in 2013, where they printed both an LFP-based cathode and an LTO-based anode onto a gold current collector (Figure 5A).^[34] Here, a printable ink was developed by dispersing lithiated electrode materials into a solution of water, ethylene glycol (EG), and glycerol. In addition, hydroxyethyl cellulose (HEC) and hydroxypropyl cellulose (HPC) were also

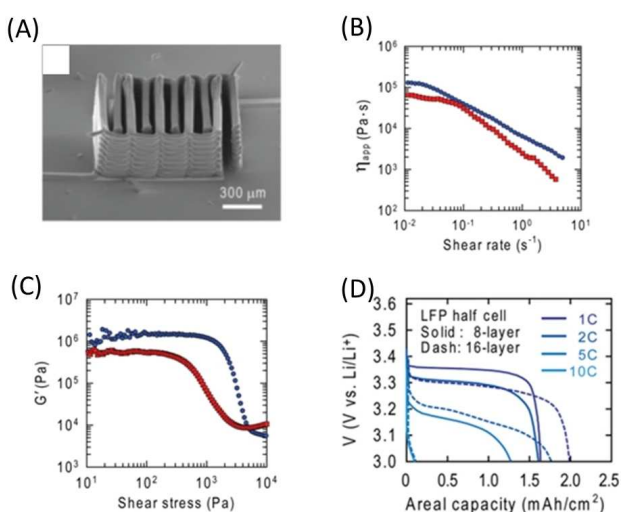


Figure 5. **A.** SEM images of printed and annealed 16-layer interdigitated LTO-LFP electrode architectures. **B.** Apparent ink viscosity as a function of shear rate for the LFP and LTO inks. **C.** Storage modulus as a function of shear stress for the LFP and LTO inks. **D.** Rate profiles of the LFP half-cell at various currents.^[34] Reproduced with permission from Ref. [34]. Copyright 2013 Wiley-VCH.

added to the electrode inks to serve as viscosifiers. In this report, Lewis and co-workers presented two prerequisites of printing inks for DIW of EES devices as follows: (i) shear-thinning behavior, and (ii) desirable viscoelastic properties. As Figure 5B shows, both electrode inks displayed high apparent viscosity and shear-thinning behavior, which reveals that they can be easily printed. Figure 5C shows storage modulus (G') of the inks as a function of shear stress. There was a dramatic drop in storage modulus when the shear stress increased from 10^2 to 10^3 Pa. These rheological parameters indicate that the inks were suitable for the DIW method.^[66]

After printing, the organic solvents were removed by heating the dried electrode arrays to 600 °C. Liquid electrolytes were filled in the gap between electrodes. The packaged 3-Dimensional Interdigitated Micro-Battery Architecture (3D-IMA) delivered higher areal energy and power densities than most traditionally manufactured lithium-ion batteries proposed earlier in the literature. It is noticeable, the 16-layer LFP exhibited higher specific capacities than the 8-layer LFP at 1 C and 2 C, but the performances of the cells were similar at 5 C and 10 C due to the weak electronic transportation (Figure 5D). The authors also suggested using conductive fillers to enhance the electronic transportation. Subsequently, the same group reported a fully 3D printed LIBs composed of thick, biphasic semisolid electrodes.^[90] With the new electrode inks made with addition of Ketjenblack carbon particles, the performances of the printed cells exhibit a significant improvement compared with the previous 3D-IMA.

Akin to the work of Sun *et al.*, Fu *et al.* proposed a similar interdigitated structures (Figure 6A).^[61] To overcome the electrical conductivity barrier, graphene oxide (GO) fillers were incorporated into the LFP cathode and LTO anode composite inks. In this case, the GO filler serves two purposes: to modify

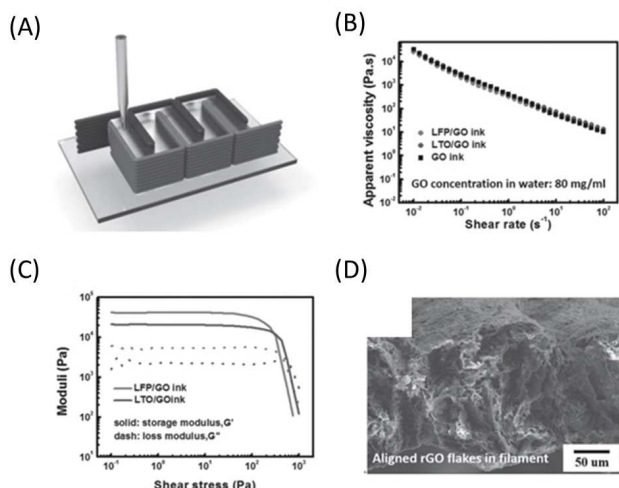


Figure 6. A. Schematic of the 3D-printed interdigitated GO-based electrodes filled with composite electrolyte ink. B. Apparent viscosity as a function of shear rate for pure GO, GO/LFP, and GO/LTO inks. C. Storage modulus and loss modulus as a function of shear stress for GO/LFP and GO/LTO inks. D. SEM image of the aligned r-GO flakes in filament.^[61] Reproduced with permission from Ref. [61]. Copyright 2016 Wiley-VCH.

the rheology of the inks and to increase the conductivity after having thermally annealed to reduced graphene oxide (r-GO). The GO based electrode inks exhibited high viscosity and shear-thinning behavior (Figure 6B). The moduli of inks have been discussed further in the report. For both inks, the storage modulus was higher than the loss modulus which indicated that the inks exhibit a solid-like behavior. After a yield point, the loss modulus is higher than storage modulus with an increase in shear stress, indicating the dominance of viscous deformation (Figure 6C).

In an interesting development, it was reported that nanoflakes can be aligned along the extrusion direction due to the high shear stress generated during the DIW processing.^[61,91–92] Fu *et al.* reported that the alignment of GO flakes provides a continuous electron pathway and enhanced electrical conductivity (Figure 6D). With these highly aligned fillers, the electrical conductivity of r-GO/LFP and r-GO/LTO electrodes after annealing improved to 31.6 and 6.1 Scm⁻¹ respectively, which are higher than those of the electrodes reported by Sun *et al.* (10⁻⁴–10⁻⁶ Scm⁻¹).

Another exemplary work proposed by Hu *et al.*, utilized an ink-based direct writing to print a specialty cathode ink onto an aluminum substrate (Figure 7A).^[32,63] This ink comprised of synthesized carbon coated LiMn_{0.21}Fe_{0.79}PO₄ (LFMP), XC-72 carbon black, and PVDF. Once printed and cured, these 3D-printed cathodes offered superior performance with capacity topping-off near 108.45 and 150.21 mAhg⁻¹ at 100 C and 10 C, respectively. The specific capacities of the cells with printed cathodes are 15%–50% higher than that of the cells with traditional electrodes at various current densities. Even more impressive was the fact that these electrodes delivered this performance for up to 1000 cycles. Compared to a traditional cathode, the 3D printed electrode delivered higher capacity from 1 C to 100 C (Figure 7B). To understand the reason behind

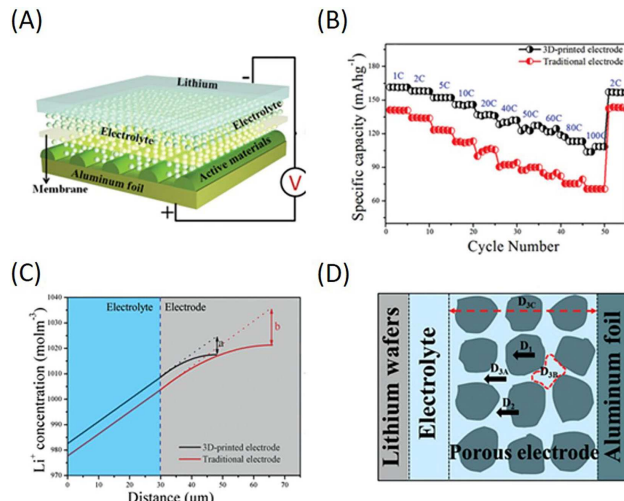


Figure 7. A. Schematic of battery preparation with the 3D-printed LiMn_{0.21}Fe_{0.79}PO₄ based electrode. B. Rate profiles of the 3D-printed and traditional electrodes.^[63] C. Relationship between Li-ion concentration and electrode thickness determined by P2D model. D. Factors influencing Li-ion transport: bulk diffusion (D₁), particle interfacial reaction (D₂), solution intrinsic diffusion coefficient (D_{3A}), efficiency porosity (D_{3B}), and electrode thickness (D_{3C}).^[63] Reproduced with permission from Ref. [63]. Copyright 2016 Wiley-VCH.

this extraordinary performance, a pseudo 2D hidden Markov model (P2D) model was applied to simulate the relationship between electrochemical performances and electrode layer thickness (Figure 7C). Other than the bulk diffusion and particle diffusion which have been reported to affect the rate performances of lithium-ion batteries, Hu *et al.* made efforts to study the effects of the electrolyte diffusion, such as solution intrinsic diffusion coefficient (D_{3A}), efficiency porosity (D_{3B}), and electrode thickness (D_{3C}) (Figure 7D). Electrodes with less printed layers delivered better rate performances because all the active materials were involved in the electrochemical reaction. However, by optimizing the efficiency porosity of electrode, electrodes with more printed layers could also be made to perform well at high rates.

A further advantage of EES devices with interdigitated structures is that it is membrane free. The anode and the cathode are separated by a width controllable gap, which can be filled with the liquid electrolytes. Hence, the cost of the EES devices can be reduced due to the fact that a membrane such glass fiber membrane or Celgard membrane is not required. However, the safety concerns of the carbonate-based liquid electrolyte have recently attracted lots of attention.^[93–94] Solid-state electrolytes have been suggested to replace liquid electrolytes owing to their outstanding properties, such as safety, stability, mechanical properties and flexibility.^[94–96] However, the high cell area-specific resistance (ASR) of solid-state electrolytes in EES devices is the major obstacle to the commercialization of solid-state EES devices.^[97] The low ionic conductivity, long diffusion distance in thick electrode and poor electrode/electrolyte contact are the main reasons caused high ASR.^[98–101] 3D printing of structured solid-state electrolytes

is now becoming increasingly attractive for EES devices to reduce the ASR.^[45,64–65, 97]

Solid-state electrolytes are typically fabricated in a flat and planar form. The thickness of conventional solid-state battery is relatively higher ($> 150 \mu\text{m}$) than that of liquid electrolytes ($\approx 25 \mu\text{m}$).^[97] The high thickness of the electrode leads to a longer lithium ion diffusion path, and this barrier is difficult to eliminate through conventional manufacturing process. McOwen *et al.* have developed multiple solid electrolyte inks using $\text{Li}_2\text{La}_3\text{Zr}_2\text{O}_{12}$ (LLZ) garnet as a model solid electrolyte material for the first time.^[97] The garnet-type LLZ based ink can be printed on a porous-dense multilayer LLZ tape substrate. After sintering, a $5\text{--}10 \mu\text{m}$ solid-state electrolyte with self-supporting interdigitated structures was created (Figure 8A). The average overpotential was 2.3 and 7.2 mV at the current density of 0.1 and 0.33 mA cm^{-2} (Figure 8B). The ASR of the cell after charge/discharge cycling ($22 \Omega \text{ cm}^2$) was even lower than that of before cycling ($38 \Omega \text{ cm}^2$), owing to its improved interfacial contact surface. Polymer-based solid-state electrolytes also have been printed by Cheng *et al.*^[65] In the work, hybrid polymer-based electrolytes were printed using a developed direct ink writing 3D printer at an elevated-temperature. The hybrid solid-state electrolyte ink was made of a polymer base containing titanium oxide particles that can improve the electrochemical and rheological properties of the ink. The electrolyte inks can be directly deposited into the battery as it is being printed. It is worth noting that a continuous, thin, and dense layer was formed between the porous electrolyte layer and the electrode (Figure 8C, D), which effectively reduced the interfacial resistance of the solid-state battery. Figure 8E shows that in comparison with the electrolytes prepared by the conventional cast method, the interfacial resistance of the printed hybrid electrolytes was smaller in the mid-frequency region. The cells with printed electrolytes displayed higher specific capacity than the cells with cast electrolytes due to the lower interfacial resistance.

In recent years, 3D printing of supercapacitors has also drawn a lot of attention due to their high power density, long

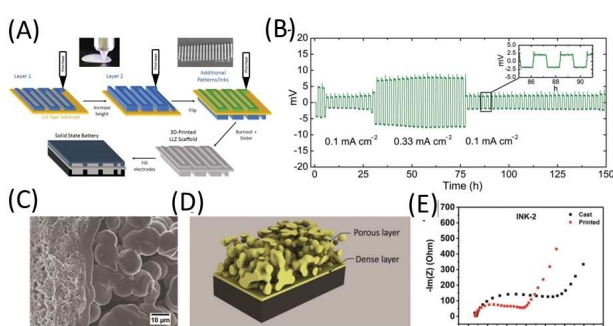


Figure 8. A. Schematic of the process to 3D-print solid electrolyte structures. B. Galvanostatic cycling of Li/LLZ/Li metal cell at various current densities.^[97] Reproduced with permission from Ref. [97]. Copyright 2018 Wiley-VCH. C. SEM and D. schematic image of the dense layer between electrolyte and electrode. E. Impedance spectra for $\alpha\text{-MnO}_2/\text{Li}$ half-cells with printed electrolyte and cast electrolyte.^[65] Reproduced with permission from Ref. [65]. Copyright 2018 Wiley-VCH.

cycle life, and even flexibility. Among them, fully packaged symmetrical interdigitated electrodes with liquid or gel polymer electrolytes is the most popular design. The major advantage of supercapacitors with the interdigitated structures is that the electrode width (w_e) and the gap between the electrodes (w_g) can be controlled well by 3D printing technique. Hence, the equivalent series resistance (ESR) can be reduced by the decreasing the ratio of w_e and w_g . Low ESR promotes both the power and energy densities.^[35,37]

Carbon materials, such as carbon nanotubes (CNTs), graphene oxide and carbon black, have been widely used in the preparation of 3D printing inks for supercapacitor applications because of their superior ink-formation ability and mechanical properties, large surface area, and high conductivity.^[102–109] However, the aggregation of CNTs and the bad dispersion due to van der Waals attractions between tubes will result in nozzle clogging during DIW processing.^[110] Hence, a suitable strategy to suspend them well in the solution without compromising on the electrical conductivity is necessary during ink preparation. Bolin *et al.* demonstrated a fully packaged single-walled carbon nanotubes (SWNTs)-based supercapacitor with DIW technology.^[111] SWNTs based electrode ink and PVA electrolyte ink were printed on a Kapton film substrate and sealed by printing a silicone rubber layer. Two electrode legs were exposed for electrical connection (Figure 9A). In this work, the SWNTs was mixed with sodium dodecyl sulfate (SDS) surfactant and subjected to high power probe sonication to disperse SWNTs in DI water uniformly. After the supercapacitor with interdigitated structures pattern has been fabricated by DIW processing, the surfactant layer on the top of electrode can be removed by acid treatment significantly (Figure 9B). The fully packaged SWNTs-based supercapacitor is flexible (Figure 9C) and performed well even when the cell was bent (Figure 9D). Figure 9E shows that the cell can maintain $\sim 96.5\%$ of its initial capacitance (15.34 F cm^{-3}) after 5000 cycles.

Shen *et al.* demonstrated a quasi-solid-state asymmetric micro-supercapacitors with ultrahigh areal energy density by DIW technology (Figure 10A).^[62] In this work, the typical

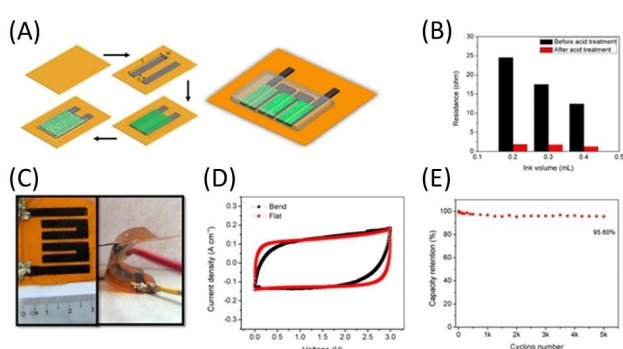


Figure 9. A. Schematic of the fully packaged SWNTs-based supercapacitor. B. Change of resistance of printed traces with ink volume used before and after nitric acid treatment. C. Optical picture of the printed supercapacitor array and bent supercapacitor array. D. CV of bent and flat cells. E. Capacitance retention of the supercapacitor at 1.32 A cm^{-3} .^[111] Reproduced with permission from Ref. [111]. Copyright 2017 American Chemical Society.

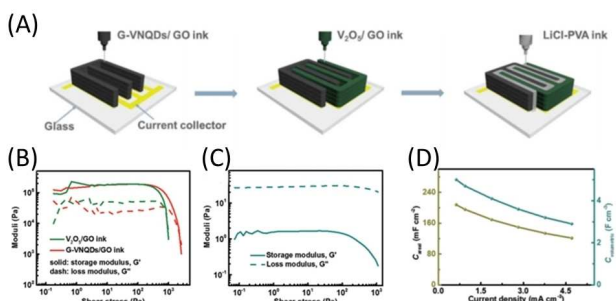


Figure 10. A. Schematic of the 3D-printed interdigitated asymmetric micro-supercapacitors. Storage modulus and loss modulus as a function of shear stress for B. V₂O₅/GO and G-VNQDs /GO inks and C. LiCl-PVA gel electrolytes. D. Corresponding areal and volumetric capacitances of the 3D printed asymmetric micro-supercapacitors.^[62] Reproduced with permission from Ref. [62]. Copyright 2018 Wiley-VCH.

cathode and anode inks are composed of vanadium pentoxide (V₂O₅) and graphene–vanadium nitride quantum dots (G-VNQDs) with highly concentrated graphene oxide (GO) dispersions, respectively. The electrodes exhibited high viscosities and shear-thinning behavior after the addition of the GO. The viscoelastic behaviors of electrode inks are similar to Fu *et al.*'s work,^[61] i.e., the storage modulus is higher than loss modulus at higher shear stress which indicated a dominate elastic behavior. After the yield point, the liquid behavior dominated which is beneficial for the extrusion process (Figure 10B). The electrolyte inks (LiCl/PVA) exhibit a dominant liquid behavior all throughout the testing range of shear stress which would facilitate the wettability of electrolyte into electrodes and enhances the performances of the printed micro-supercapacitors (Figure 10C). The asymmetric micro-supercapacitor with interdigitated electrodes and an electrolytes with good wettability showed a large areal mass loading of 3.1 mg cm⁻², and a wide electrochemical potential window of 1.6 V. The asymmetric micro-supercapacitors delivered areal capacitance and volumetric capacitance of 207.9 mF cm⁻² and 5.0 F cm⁻³ respectively (Figure 10D). The areal capacitance of the printed interdigitated asymmetric micro-supercapacitors is ten times higher than that of laser-writing asymmetric micro-supercapacitors.^[112]

Compared with the conventional interdigitated structures, the interdigitated micropillar arrays have been rarely employed in the 3D printing of EES devices. To maximize the advantage of 3D printing high-aspect-ratio electrode, Zhao *et al.* assembled a micro-supercapacitor with interdigitated micropillar arrays electrodes using the SLS method (Figure 11A).^[113] The micro-supercapacitor assembled with interdigitated micropillar arrays delivered an areal energy density of 2.98×10^{-6} Wh cm⁻² (Figure 11B), which was higher than the 0.92×10^{-6} Wh cm⁻² value obtained for the supercapacitor with same materials of electrodes and electrolytes in planar structure.^[114] The enhanced performance was attributed to the ultrahigh aspect-ratio in interdigitated micropillar arrays electrodes. The supercapacitor with printed electrodes also delivered a good cycling stability with 78% capacitance retention after 1000 cycles

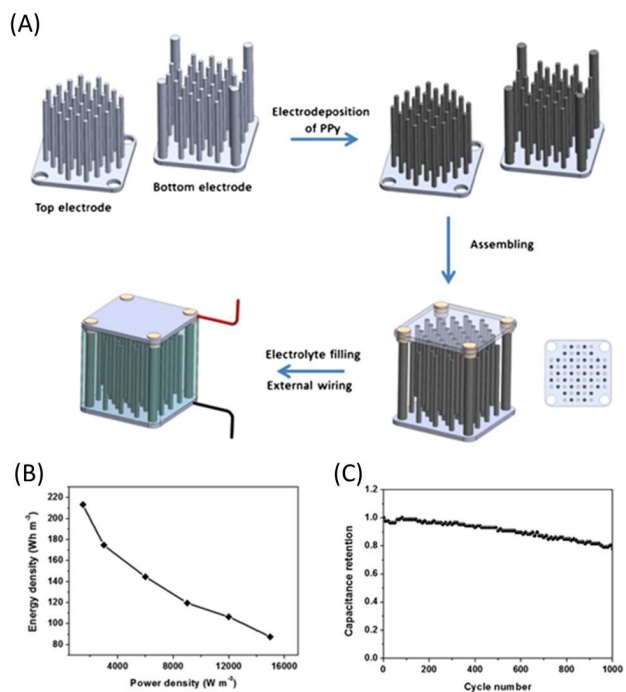


Figure 11. A. Schematic of the printing process of 3D printed interdigitated micropillar array micro-supercapacitor. B. Ragone plot of the printed micro-supercapacitor with interdigitated micropillar array architectures. C. Capacitance retention of the 3D micropillar array micro-supercapacitor.^[113] Reproduced with permission from Ref. [113]. Copyright 2014 Elsevier.

(Figure 11C), which was higher than previously reported results of planar supercapacitor.^[115]

3.2. 3D scaffolds

In the 3D scaffolds, layers of electrode or electrolyte rods are stacked in a sequence, which possess periodic macro-pores along a vertical direction.^[116] These aligned pores are known to facilitate ion-diffusion and liquid electrolyte infiltration. In addition, using a thick electrode with 3D scaffolds has been reported as a promising method to improve both energy density and power density at device-level with high areal active materials mass loading.^[90,117]

The Li-air battery system has caught the eye of this technology due to its attractive theoretical specific capacity and energy density.^[118] However, several bottlenecks, such as high charge overpotential, low recyclability, and poor rate capability have limited the application of this technology.^[118–119] The drawbacks can be addressed by developing cathode with porous structure, good electronic and ionic conductivities, and a design that improves gas transportation during discharge.^[118] Recently, the cathode of Li-air battery has been fabricated within a high porosity architecture through 3D printing technique and addressed the drawbacks of Li-air batteries.

Lacey *et al.* added holey graphene oxide (hGO) to green solvents, such as water, to make 3D-printable inks. The additive-free inks with appropriate rheology could be used to print Li-O₂ cathodes with 3D scaffolds architectures via the DIW

method (Figure 12A).^[43] The hydrophilic hGO was synthesized from graphene powder by using purely oxidative process and liquid-phase oxidation. With the synthesis method, the hGO is inherently nanoporous with 4–25 nm through-holes. The enabled the electrode inks with high concentration hGO to be extruded into 3D scaffolds with trimodal porosity nanoscale (through-holes on hGO sheets) (Figure 12A), microscale (lyophilization-induced micropores on the printed filaments) (Fig-

ure 12B), and macroscale (pores of mesh design) (Figure 12C). The multi-sized pores enabled efficient transfer of oxygen, electrolytes and the ions. Hence, after the thermal reduction of hGO to r-hGO, the 3D printed electrodes with 3D scaffolds delivered an excellent areal capacitance of 13.3 mAh cm^{-2} at 0.1 mA cm^{-2} (Figure 12D), which was much higher than the areal capacitance of a coin cell 0.21 mAh cm^{-2} with 2D electrode.

Lately, Qiao *et al.* demonstrated an ultrathick cathode ($\approx 0.4 \text{ mm}$) composed of Ni nanoparticles which are anchored on a 3D printing of 3D scaffolds r-GO by thermal shock treatment (Figure 13A).^[44] Firstly, a GO 3D scaffold was built by the DIW method. Then, the GO was reduced in argon gas at 300°C to obtain the r-GO 3D scaffolds. The r-GO 3D scaffolds were dipped into NiCl_2 solution followed by thermal shock heating (1900 K) to anchor Ni nanoparticles on the r-GO 3D scaffolds. In this process, the ultrafine catalyst Ni nanoparticles ($\approx 5 \text{ nm}$) were distributed uniformly on the surface of the r-GO 3D scaffolds (Figure 13B, C). As Figure 13D shows, the $\text{Li}-\text{O}_2$ with the ultrathick cathode of r-GO/Ni 3D scaffolds shows a high specific capacity (limited to 1000 mAh g^{-1}) at 100 mA g^{-1} , a high areal capacity of $14.6 \text{ mA h cm}^{-2}$, owing to the r-GO 3D scaffolds and uniform distribution of the Ni nanoparticles. Additionally, a relatively low overpotential (1.36 V) at a current density of 200 mA g^{-1} was observed as shown in Figure 13E, which is much lower than that of previous reports at the same current density.^[120–121]

The electrodes of supercapacitors can also be printed as the 3D scaffolds. Developing 3D graphene aerogels that possess interconnected graphene networks, has been considered as a novel strategy to provide additional ion-accessible pathway and facilitate efficient ion diffusion during charge/discharge.^[122–125] Zhu *et al.* demonstrated 3D printing of graphene aerogel microlattices through DIW technique with a developed printable GO ink.^[122] The 3D aerogel microlattices maintained the properties of a single graphene sheet and exhibited supercompressibility, a large surface area, and a low relative density. However, their high electrical resistance limited their application in EES devices. Therefore, to improve the electrical conductivity and printability of the initial GO ink, Zhu *et al.* incorporated graphene nanoplatelets (GNP) and SiO_2 with an optimized loading into the ink. The supercapacitors assembled with the printed electrodes delivered an excellent rate capability and capacitance retention.^[124] In addition, Tang *et al.* synthesized versatile graphene aerogel (GA) and graphene mixed-dimensional hybrid aerogel (MDHA) based inks which can be used for integration of multiple negatively charged materials for 3D printing purposes (Figure 14A).^[126] The versatile hybrid inks overcame the barriers of multi-component inhomogeneity and harsh post-treatments requirements for the removal of additives. The printed supercapacitor exhibited a quasi-rectangular shaped cyclic voltammetry curves at various sweep rates (Figure 14B). The supercapacitor with the printed 3D scaffolds electrode delivered an areal capacitance of $639.56 \text{ mF cm}^{-2}$ at 4 mA cm^{-2} and retained 71.4% at 40 mA cm^{-2} (Figure 14C). The good rate performance is contributed by the unique structure. For conventional thick-film

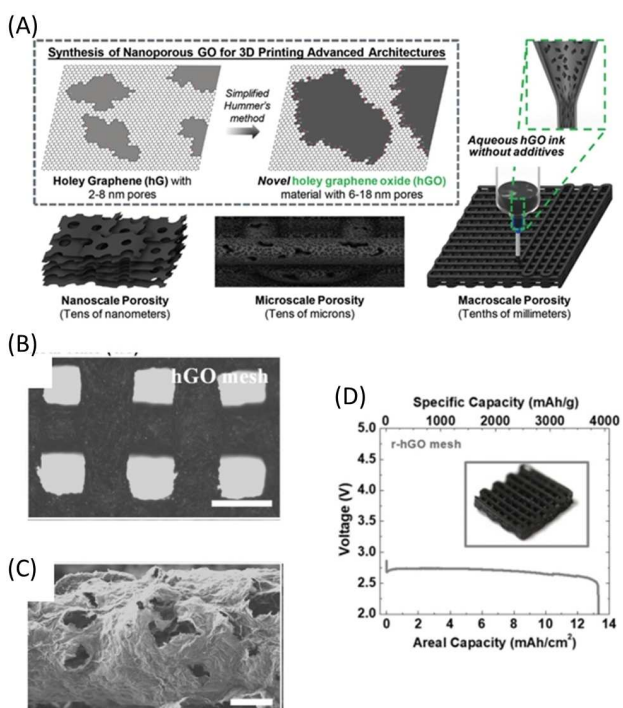


Figure 12. A. Schematic representation of the processes used to synthesize highly porous 2D nanomaterial hGO and the 3D printing of aqueous hGO ink for 3D scaffolds electrode. B. Optical image of the freeze-dried hGO mesh structure. Scale bar is $500 \mu\text{m}$. C. SEM image of the hierarchically porous 3D printed hGO mesh structure. Scale bar is $50 \mu\text{m}$. D. Deep discharge performance of the 3D printed $\text{Li}-\text{O}_2$ cathodes comprised of hierarchically porous r-hGO 3D scaffolds.^[43] Reproduced with permission from Ref. [43]. Copyright 2018 Wiley-VCH.

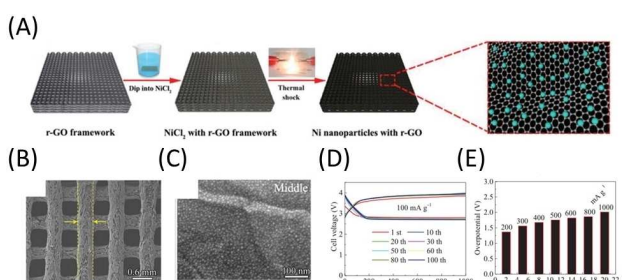


Figure 13. A. Schematic of the synthesis of the 3D-printed r-GO based electrode with 3D scaffolds, featuring thermal shock synthesized Ni nanoparticles. SEM image of 3D printed Ni/r-GO 3D scaffolds in B. the top-section and C. the middle cross section. D. Charge and discharge curves of the 3D printed Ni/r-GO 3D scaffolds as the cathode at a current density of 100 mA g^{-1} . E. The corresponding overpotential of the cathode at various current densities.^[44] Reproduced with permission from Ref. [44]. Copyright 2018 Wiley-VCH.

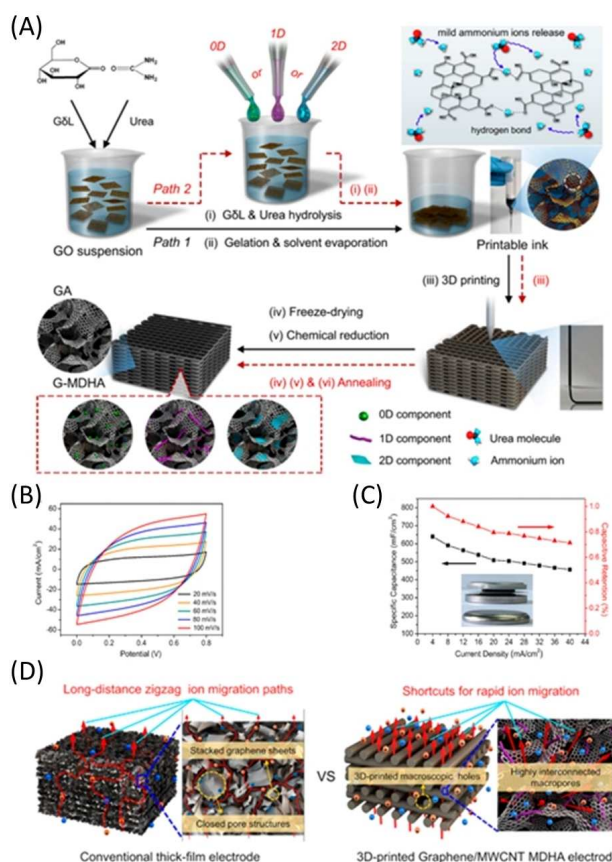


Figure 14. A. Schematic of preparation of GA and graphene MDHA based ink and printing process. B. CV profiles of supercapacitor with graphene/MWCNT MDHA at various sweep rates. C. Areal capacitance and capacitive retention versus different areal current densities. D. Schematic illustrations of insufficient ion migrations for a conventional thick-film electrode and sufficient ion migrations for the 3D-printed electrode.^[126] Reproduced with permission from Ref. [126]. Copyright 2018 American Chemical Society.

electrodes, the ions pass through a long zigzag path through the electrodes (Figure 14D). In contrast, unobstructed channels for ion transport from the bottom to top surface could be provided by the 3D printed electrodes with 3D scaffolds (Figure 14D).

Besides 3D scaffolds, Zekoll *et al.* fabricated a series of complex 3D structured (ordered cubic, gyroidal, diamond-shaped) hybrid electrolytes, which were composed of ceramic Li_{1.4}Al_{0.4}Ge_{1.6}(PO₄)₃ (LAGP) and on-conducting polypropylene (PP) or epoxy polymer (epoxy) (Figure 15A).^[45] A 3D structured polymer template was fabricated using the SLA method. Then, LAGP powders were sintered to yield the negative replication of the 3D structured polymer templates. The structured LAGP scaffolds were obtained after the removal of the polymer template by calcination in air. The hybrid electrolytes were then fabricated by filling structured LAGP scaffold with the polymer (polypropylene or epoxy). Figure 15B displays the SEM images of the structured LAGP scaffolds with cube, gyroid, diamond and bijel-derived microarchitectures. The electrochemical performances and mechanical properties of the hybrid electrolytes were influenced by the microarchitecture. Among the hybrid electrolytes, the LAGP epoxy electrolytes

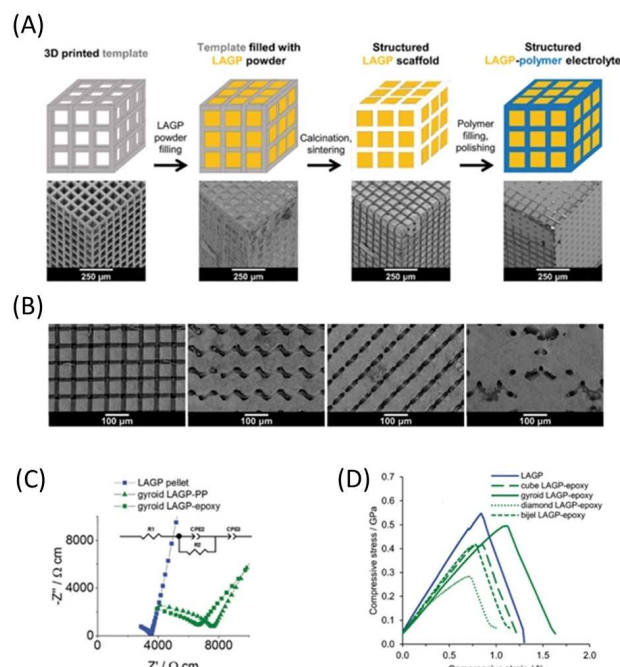


Figure 15. A. Schematic of the synthesis of structured hybrid electrolytes. B. SEM images of the structured LAGP scaffolds. C. Electrochemical impedance spectroscopy test of the structured LAGP-epoxy electrolytes. D. Stress-strain curves of LAGP and structured hybrid electrolytes with epoxy polymer.^[45] Reproduced with permission from Ref. [45]. Copyright 2018 Royal Society of Chemistry.

with gyroidal microarchitecture delivered the highest ionic conductivity of 1.6×10^{-4} S cm⁻¹ at room temperature (Figure 15C) and the best galvanostatic cycling performance. The LAGP epoxy electrolytes with gyroidal microarchitecture also displayed a large improvement in mechanical properties in compared with the LAGP pellets (Figure 15D).

3.3. Fibers

In order to further facilitate the portability of EES devices portability, the trend shifted towards developing light, thin, flexible and wearable devices, since at present, the most commercial EES devices cannot reach these requirements. Currently, research efforts are devoted to various materials and design to enable sufficient flexibility.^[127–129] The obstacles hindering the commercialization of light and wearable EES devices are fabrication cost, efficiency, and scalability.^[33]

Hu and co-workers demonstrated an all-fiber quasi-solid-state lithium ion battery using the direct ink writing method.^[33] As Figure 16A shows, LFP or LTO particles were mixed with PVDF (binder) and CNTs (conductive additive) in NMP to make electrode slurry. Printed fibers had been twisted with yarn, after which multiple yarns were twisted together and assembled into a heat-shrinkable tube. The all all-fiber quasi-solid-state lithium ion battery delivered stable charge/discharge curves with a constant overpotential of 0.18 V (Figure 16B). Due to the highly integrated twisted fiber configuration, good flexibility and stability are expected. Moreover, even when manually

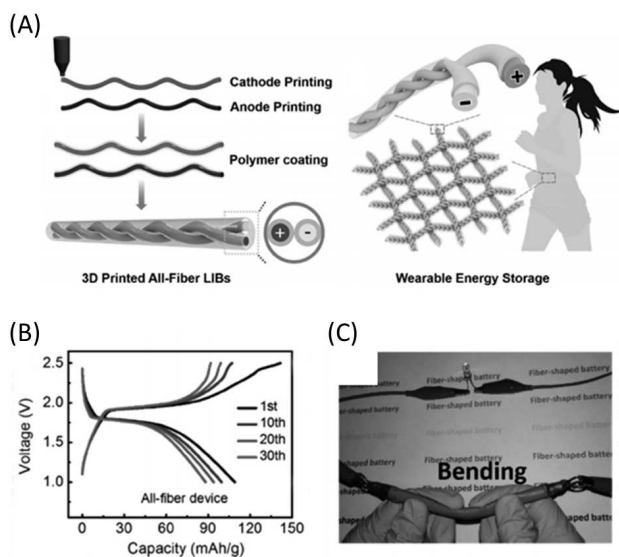


Figure 16. A. Schematic of the design concept, fabrication process and potential application of 3D printed fiber LIBs. B. Charge and discharge profiles of the fiber LIB. C. Demonstration of the fiber LIB lighting up a LED in a bent state.^[33] Reproduced with permission from Ref. [33]. Copyright 2017 Wiley-VCH.

bending the device for several minutes, the brightness of LED powered by this battery did not change (Figure 16C).

The same group also developed a polymer matrix by adding boron nitride nanosheet (BNNS) to improve the thermal transport properties for 3D printing of thermal regulation textile (Figure 17A).^[92] The alignment and homogenous dispersion of BNNSs are the key factors to take advantage of in-plane thermal transport of BNNSs. In this work, the BNNSs were dispersed in a solution of PVA by sonication. It is worth noting that the nanosheets could be aligned along the extruding direction during the printing process owing to the high shear stress induced by the printer nozzle.^[61,91-92] The printed PVA/BNNS composite fiber was further processed by hot-drawing to well orient the BNNSs and obtain the aligned BNNS/PVA (a-BNNS/PVA) composite. The thermal conduction of the a-BNNS/PVA composite fiber had been improved since a number of thermally conductive pathways were formed along the orientation of aligned BNNSs. The a-BNNS /PVA fabric displayed a high thermal conductivity of 0.078 W/(m·K), which is ~2.2 and ~1.6 times higher than that of the cotton fabric and PVA fabric, respectively (Figure 17B). On the other hand, the mechanical properties of the a-BNNS/PVA composite fiber were also enhanced by the well-aligned BNNSs. The stiffness of the a-BNNS/PVA fabric is 12.38 GPa, which is ~57 times higher than that of pure PVA fiber (Figure 17C).

Subsequently, the studies of BNNSs have been extended to the application of the 3D printing of thermal management separator for Li-ion batteries by the same group (Figure 17D).^[130] Compared with the cell with a commercial separator, the PVDF-co-HFP/BNNS composite separator presented a more stable voltage curve with a smaller overpotential for 500 h (Figure 17E). The results indicated that the PVDF-co-

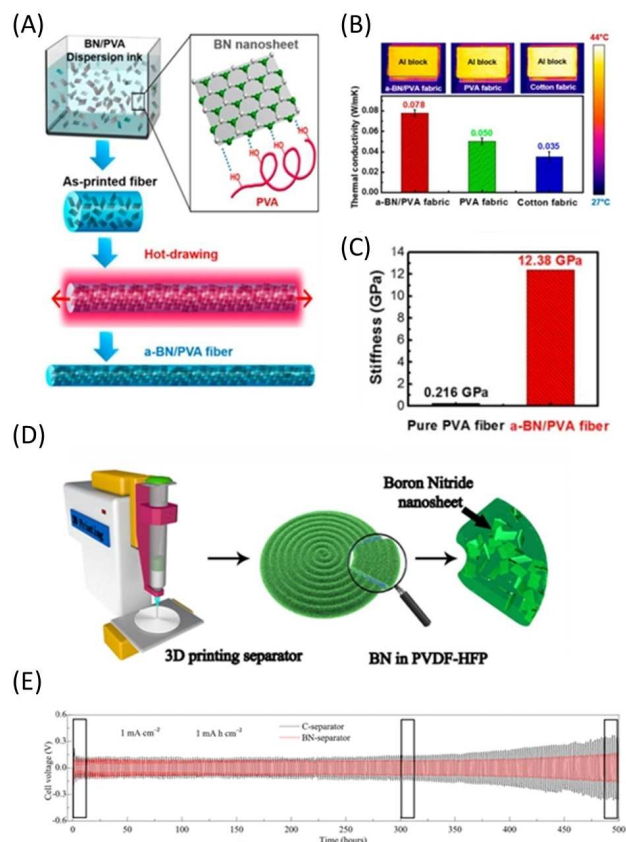


Figure 17. A. Schematic of the fabrication process of a-BNNS/PVA composite fiber. B. Measurements of the thermal conductivities of the cotton, PVA, and a-BNNS/PVA fabrics. C. Stiffness of the pure PVA and a-BNNS/PVA fiber, respectively.^[92] Reproduced with permission from Ref. [92]. Copyright 2017 American Chemical Society. D. Schematic of 3D printed PVDF-co-HFP/BNNS composite separator. E. Voltage profile of the Li/Li symmetric cells with PVDF-co-HFP/BNNS composite separator and control separator at current density of 1 mA cm⁻².^[130] Reproduced with permission from Ref. [130]. Copyright 2018 Elsevier.

HFP/BNNS composite separator could suppress the formation of lithium dendrites during long-term cycling.

Lately, Zhao *et al.* developed a fibers asymmetric supercapacitor with a maximum operating voltage of 1.6 V.^[49] The single-walled carbon nanotube (SWCNT)/V₂O₅ fiber cathode and an SWCNT/VN fiber anode were printed via direct ink writing 3D printer and then twisted to assembled as the supercapacitor (Figure 18A). The highest specific capacitance of the fiber-shaped asymmetric supercapacitor was 116.19 mF cm⁻² at a current density of 0.6 mA cm⁻² (Figure 18B).

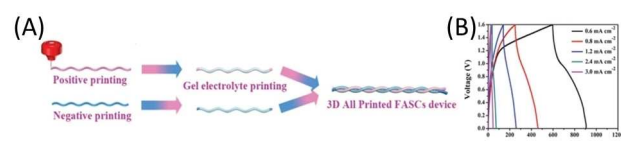


Figure 18. A. Schematic of printing process of 3D printed fibers asymmetric supercapacitors. B. Galvanostatic charge/discharge profile of the assembled FASCs at various current densities.^[49] Reproduced from Ref. [49]. Licensed under CC BY 4.0.

| Table 2. 3D-printing of rechargeable battery configurations. | | | | | | |
|--|-------|---|----------------------------------|-----------------|---------------------------|--|
| Cathode | Anode | Electrolyte | Additive | Printing method | Architecture | Specific Capacity (mAh g ⁻¹) |
| LFP | LTO | 1 M LiClO ₄ in EC:DMC | Ethylene glycol/glycerol/HPC/HEC | DW | Interdigitated structures | 116 (at 0.5 C) |
| LFP | LTO | 1 M LiPF ₆ in EC:DEC | GO | DW | Interdigitated structures | 110 (at 50 mA g ⁻¹) |
| LiMn _{0.12} Fe _{0.79} PO ₄ @C | Li | 1 M LiPF ₆ in EC:DEC | XC-72 carbon black/PVDF | DW | Interdigitated structures | 161.36 (at 1 C) |
| LFP | Li | 1 M LiClO ₄ in EC:PC | GPE/Super P | SLA | – | [63] |
| CO ₂ | Li | LiTFSI in TEGDME | rGO/Ni frame | DW | 3D scaffolds | [78] |
| O ₂ | Li | 1 M LiTFSI in DMSO | hGO frame | DW | 3D scaffolds | [44] |
| Li | Li | Li _{1-x} Al _x Ge _{1-x} (PO ₄) ₃ | Epoxy | SLA | 3D scaffolds | [43] |
| LFP | LTO | 1 M LiPF ₆ EC:DEC 1:1 | CNT/PVDF | DW | Fibers | [45] |
| | | | | | | [33] |
| | | | | | | [34] |

The highest areal energy density ($41.28 \mu\text{Wh cm}^{-2}$) and power density ($480 \mu\text{W cm}^{-2}$) of the 3D printed fibers asymmetric supercapacitors are much higher than that of reported fiber-shape supercapacitors.^[131–134]

4. Comparison of 3D Printing of EES Devices with Various Architectures

Although 3D-printing of batteries has not yet fully made its way into the manufacturing community, it is important to categorize and summarize the accomplished work to get a perspective of the challenges that need to be addressed. In this section, the 3D-printed EES devices have been categorized into rechargeable batteries (Table 2), and supercapacitors (Table 3). Ragone plots of the reported devices fabricated using various architectures (Figure 19A, B) are also drawn to compare their performances. The tables and figures below depict the major EES devices made with additive manufacturing techniques.

The Ragone plot shows a summary of energy density and power density for 3D printed EES devices with different architectures. As can be seen from Figure 19A, the Li-ion

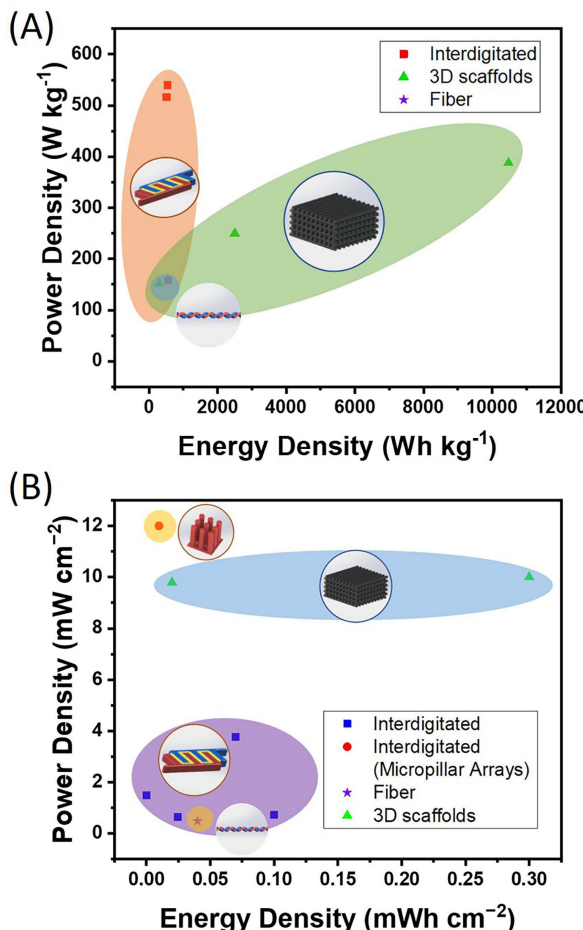


Figure 19. Ragone plots of 3D printed A. Li-ion batteries and B. supercapacitors with different architectures.

Table 3. 3D-printing of supercapacitor configurations.

| Electrode | Electrode | Electrolyte | Additive | Printing method | Architecture | Capacitance (mF cm ⁻²) | Reference |
|---|---|--|--------------------------------|-----------------|---|--------------------------------------|-----------|
| V ₂ O ₅ | G-VNQDs | LiCl-PVA | GO | DIW | Interdigitated structures | 207.9 (at 0.63 mA cm ⁻²) | [2] |
| SW-CNT | SW-CNT | LiCl-PVA | H ₂ SO ₄ | DIW | Interdigitated structures | 1.93 (at 3.2 mA cm ⁻³) | [11] |
| GO | GO | PVA-H ₂ SO ₄ | PANI | DIW | 3D scaffolds /Interdigitated structures | 1329 (at 5 mA cm ⁻²) | [135] |
| Ti ₃ C ₂ T _x | Ti ₃ C ₂ T _x | Mn(C ₂ H ₃ O) ₂ | — | DIW | Interdigitated structures | 61 (at 0.025 mA cm ⁻²) | [136] |
| Graphene aerogel/MnO ₂ | Graphene aerogel/MnO ₂ | PVA-KOH | — | DIW | 3D scaffolds | 44.13 (at 0.5 mA cm ⁻²) | [125] |
| GO/NiO | GO/NiO | PVA-KOH | — | DIW | Interdigitated structures | 166.6 (at 0.6 mA cm ⁻²) | [108] |
| GO/Co ₉ O ₄ | GO/Co ₉ O ₄ | LiCl-PVA | — | SLS | Interdigitated structures | 199.2 (at 1.15 mA cm ⁻²) | [109] |
| Polymide | Polymide | PVA-H ₃ PO ₄ | Polypyrrole | SLS | Interdigitated structures | 42.6 (at 0.1 mA cm ⁻²) | [137] |
| Ti ₆ Al ₄ V | Ti ₆ Al ₄ V | PVA-KOH | SW-CNT/PVA | DIW | Interdigitated Micropillar Arrays | 1920 (at 3.74 mA cm ⁻³) | [113] |
| V ₂ O ₅ | V ₂ O ₅ | V ₂ O ₅ | V ₂ O ₅ | Fibers | Fibers | 116.19 (at 0.6 mA cm ⁻²) | [64] |

batteries with interdigitated structures and 3D scaffolds outperform 3D fibers battery in terms of both energy density and power density. The high performance of the printed interdigitated structures culminates from the high aspect ratio structures and considerably narrow electrode spacing, which are characteristics that augment ion and electron transport during the charging and discharging processes.^[34] In addition, the batteries with 3D scaffolds present extremely high energy density, which can be attributed to two factors: Firstly, the micro-scale pores enable entire active-site utilization to dramatically improve Li-O₂ battery performance. Secondly, thicker electrodes with efficiency porosity delivers higher performance compared with that of thin electrodes.

The performance of supercapacitors with the architectures is similar to that of Li-ion batteries (Figure 19B). Most of the interdigitated and 3D scaffolds structured supercapacitors deliver higher energy and power densities than those of fibers supercapacitors. However, it is not possible to draw a conclusion at this point due to lack of sufficient data.

5. Conclusions and Challenges

Compared with traditional manufacturing methods, 3D printing techniques exhibit several advantages, especially in terms of cost, scalability and sustainability. One of the major benefits in using 3D printing technique is the design flexibility and having that advantage not only promotes the energy density and power density but also enables the development of EES devices for wearable devices. We have reviewed three primary architectures widely used in 3D printing of EES devices, namely interdigitated structures, 3D scaffolds, and fibers.

Here, the challenges involved in the fabrication of EES devices with different 3D architectures and 3D printing techniques are summarized in Figure 20. Complex 3D structures, such as interdigitated micropillar arrays and 3D scaffolds, need to be printed with high resolution, accuracy, and surface finish. This is because the EES devices can be easily short circuited if the electrodes cannot be printed through the design route, and open circuit may be caused if the solid-state

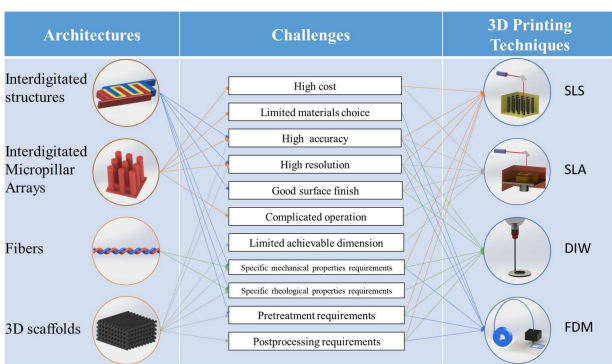


Figure 20. Schematic illustrating the prominent features and challenges of the different architectures and processes involved in 3D printing of EES devices.

electrolytes are not printed exactly between the electrodes. Both situations are likely to occur during the fabrication of micro-scale EES devices. From the materials perspective, desired rheological property is a prerequisite to achieve high resolution 3D architectures using direct ink writing method. Although adding fillers have been reported as a promising method to optimize rheological properties without losing performance, post-processing steps such as high-temperature heat treatment and freeze-drying are required after printing, which will increase the cost, and complicate the manufacturing operations. For interdigitated micropillar arrays, the storage modulus of printed materials needs to be high enough for them to be self-supporting. On the technological side, complex 3D structures can also be produced by adopting advanced 3D printers, which provide higher resolution, operating pressure and temperature, smaller laser spot size, etc.

The material processing is another challenge in the development of 3D printing of EES devices. For the DIW, a wide range of active materials can be used as inks for 3D printing, but the printing inks need to meet a desired rheological property behavior, a requirement that could be met by adding filler materials. The SLA method requires the addition of a high concentration of photoinitiators to render the material UV curable. However, the photoinitiators make no contribution to the electrochemical performance of EES devices. The FDM is potentially one of the most attractive techniques for fabricating commercial 3D printing of EES devices. It requires the use of thermoplastics which are indispensable materials to make the filament extrudable at elevated temperatures. The thermoplastics, with their low ionic conductivities, would substantially reduce the performances of EES devices.

Integrating 3D printed EES devices with interdigitated structures and 3D scaffolds into electronic device manufacturing is another potential application. Nevertheless, fully printing EES devices is a further challenge. Typically, there are at least three individual components to form EES devices but most of the 3D printing methods can only print one material at a time. There is a diversity of potential for multi-material printing methods, such as direct ink writing and fused deposition modeling to achieve the goal. Inks or filaments of the electrodes, electrolytes and highly conductive non-metallic current collectors would also need to be well designed.

Acknowledgements

R.S.-Y., M.C., and R.D. acknowledge the financial support from NSF award CBET-1805938. R.D.'s efforts were supported by NSF award no. DMR-1809439. R.S.-Y., M.C., and R.D. acknowledge the Battery Technology Laboratory of the College of Engineering at the University of Illinois at Chicago (UIC). M.C. acknowledges China Scholarship Council (CSC). M.C. acknowledges Jared Morrisette for his assistance with organizing the references and figures.

Conflict of Interest

The authors declare no conflict of interest.

Keywords: 3D printing • electrochemical energy storage devices • batteries • supercapacitors

- [1] J. M. Tarascon, M. Armand, *Nature* **2001**, *414*, 359–367.
- [2] M. Wakihara, *Mater. Sci. Eng. R* **2001**, *33*, 109–134.
- [3] X. Tian, J. Jin, S. Yuan, C. K. Chua, S. B. Tor, K. Zhou, *Adv. Energy Mater.* **2017**, *7*, 1700127.
- [4] G. Wang, L. Zhang, J. Zhang, *Chem. Soc. Rev.* **2012**, *41*, 797–828.
- [5] I. Hadjipaschalidis, A. Poulikkas, V. Efthimiou, *Renewable Sustainable Energy Rev.* **2009**, *13*, 1513–1522.
- [6] B. Wang, J. B. Bates, F. X. Hart, B. C. Sales, R. A. Zuhr, J. D. Robertson, *J. Electrochem. Soc.* **1996**, *143*, 3203–3213.
- [7] H. Xia, L. Lu, G. Ceder, *J. Power Sources* **2006**, *159*, 1422–1427.
- [8] K. A. Striebel, C. Z. Deng, S. J. Wen, E. J. Cairns, *J. Electrochem. Soc.* **1996**, *143*, 1821–1827.
- [9] Y. Iriyama, M. Inaba, T. Abe, Z. Ogumi, *J. Power Sources* **2001**, *94*, 175–182.
- [10] Z.-S. Wu, K. Parvez, X. Feng, K. Müllen, *J. Mater. Chem. A* **2014**, *2*, 8288–8293.
- [11] W. Zhou, C. Cheng, J. P. Liu, Y. Y. Tay, J. Jiang, X. T. Jia, J. X. Zhang, H. Gong, H. H. Hng, T. Yu, H. J. Fan, *Adv. Funct. Mater.* **2011**, *21*, 2439–2445.
- [12] D. Manfredi, F. Calignano, M. Krishnan, R. Canali, E. Ambrosio, E. Atenzi, *Materials* **2013**, *6*, 856–869.
- [13] M. Gebler, A. J. S. Uiterkamp, C. Visser, *Energy Policy* **2014**, *74*, 158–167.
- [14] N. Guo, M. C. Leu, *Front. Mech. Eng.* **2013**, *8*, 215–243.
- [15] S. H. Huang, P. Liu, A. Mokasdar, L. Hou, *Int. J. Adv. Manuf. Technol.* **2012**, *67*, 1191–1203.
- [16] J. H. Martin, B. D. Yahata, J. M. Hundley, J. A. Mayer, T. A. Schaedler, T. M. Pollock, *Nature* **2017**, *549*, 365.
- [17] A. Vyatskikh, S. Delalande, A. Kudo, X. Zhang, C. M. Portela, J. R. Greer, *Nat. Commun.* **2018**, *9*, 593.
- [18] R. Trombetta, J. A. Inzana, E. M. Schwarz, S. L. Kates, H. A. Awad, *Ann. Biomed. Eng.* **2017**, *45*, 23–44.
- [19] X. Wang, M. Jiang, Z. Zhou, J. Gou, D. Hui, *Composites Part B* **2017**, *110*, 442–458.
- [20] S. J. Leigh, R. J. Bradley, C. P. Purssell, D. R. Billson, D. A. Hutchins, *PLoS One* **2012**, *7*, e49365.
- [21] J. A. Inzana, D. Olvera, S. M. Fuller, J. P. Kelly, O. A. Graeve, E. M. Schwarz, S. L. Kates, H. A. Awad, *Biomaterials* **2014**, *35*, 4026–4034.
- [22] F. P. W. Melchels, M. A. N. Domingos, T. J. Klein, J. Maldá, P. J. Bartolo, D. W. Hutmacher, *Prog. Polym. Sci.* **2012**, *37*, 1079–1104.
- [23] H. N. Chia, B. M. Wu, *J. Biol. Eng.* **2015**, *9*, 4.
- [24] A. D. Valentine, T. A. Busbee, J. W. Boley, J. R. Raney, A. Chortos, A. Kotikian, J. D. Berrigan, M. F. Durstock, J. A. Lewis, *Adv. Mater.* **2017**, *29*, 1703817.
- [25] J. T. Muth, D. M. Vogt, R. L. Truby, Y. Mengüç, D. B. Kolesky, R. J. Wood, J. A. Lewis, *Adv. Mater.* **2014**, *26*, 6307–6312.
- [26] S. V. Murphy, A. Atala, *Nat. Biotechnol.* **2014**, *32*, 773.
- [27] M. S. Mannoor, Z. Jiang, T. James, Y. L. Kong, K. A. Malatesta, W. O. Soboyejo, N. Verma, D. H. Gracias, M. C. McAlpine, *Nano Lett.* **2013**, *13*, 2634–2639.
- [28] F. Bos, R. Wolfs, Z. Ahmed, T. Salet, *Virtual and Physical Prototyping* **2016**, *11*, 209–225.
- [29] C. Gosselin, R. Duballet, P. Roux, N. Gaudilliére, J. Dirrenberger, P. Morel, *Mater. Des.* **2016**, *100*, 102–109.
- [30] R. R. Kohlmeyer, A. J. Blake, J. O. Hardin, E. A. Carmona, J. Carpene-Nunez, B. Maruyama, J. D. Berrigan, H. Huang, M. F. Durstock, *J. Mater. Chem. A* **2016**, *4*, 16856–16864.
- [31] A. J. Blake, R. R. Kohlmeyer, J. O. Hardin, E. A. Carmona, B. Maruyama, J. D. Berrigan, H. Huang, M. F. Durstock, *Adv. Energy Mater.* **2017**.
- [32] J. T. Hu, Y. Jiang, S. H. Cui, Y. D. Duan, T. C. Liu, H. Guo, L. P. Lin, Y. Lin, J. X. Zheng, K. Amine, F. Pan, *Adv. Energy Mater.* **2016**, *6*, 8.
- [33] Y. Wang, C. Chen, H. Xie, T. Gao, Y. Yao, G. Pastel, X. Han, Y. Li, J. Zhao, K. K. Fu, L. Hu, *Adv. Funct. Mater.* **2017**, *27*, 1703140.
- [34] K. Sun, T. S. Wei, B. Y. Ahn, J. Y. Seo, S. J. Dillon, J. A. Lewis, *Adv. Mater.* **2013**, *25*, 4539–4543.

- [35] N. Liu, Y. Gao, *Small* **2017**, *13*, 1701989.
- [36] H. Zheng, J. Li, X. Song, G. Liu, V. S. Battaglia, *Electrochim. Acta* **2012**, *71*, 258–265.
- [37] H. Li, J. Liang, *Adv. Mater.* **2019**, 1805864.
- [38] X. Pu, L. Li, H. Song, C. Du, Z. Zhao, C. Jiang, G. Cao, W. Hu, Z. L. Wang, *Adv. Mater.* **2015**, *27*, 2472–2478.
- [39] Z. Gao, N. Song, Y. Zhang, X. Li, *Nano Lett.* **2015**, *15*, 8194–8203.
- [40] X. Pu, L. Li, M. Liu, C. Jiang, C. Du, Z. Zhao, W. Hu, Z. L. Wang, *Adv. Mater.* **2016**, *28*, 98–105.
- [41] D. Pech, M. Brunet, P.-L. Taberna, P. Simon, N. Fabre, F. Mesnilgrente, V. Conédéra, H. Durou, *J. Power Sources* **2010**, *195*, 1266–1269.
- [42] R. E. Sousa, C. M. Costa, S. Lanceros-Mendez, *ChemSusChem* **2015**, *8*, 3539–3555.
- [43] S. D. Lacey, D. J. Kirsch, Y. Li, J. T. Morgenstern, B. C. Zarket, Y. Yao, J. Dai, L. Q. Garcia, B. Liu, T. Gao, S. Xu, S. R. Raghavan, J. W. Connell, Y. Lin, L. Hu, *Adv. Mater.* **2018**, *30*, e1705651.
- [44] Y. Qiao, Y. Liu, C. Chen, H. Xie, Y. Yao, S. He, W. Ping, B. Liu, L. Hu, *Adv. Funct. Mater.* **2018**, *28*, 1805899.
- [45] S. Zekoll, C. Marriner-Edwards, A. K. O. Hekselman, J. Kasemchainan, C. Kuss, D. E. J. Armstrong, D. Cai, R. J. Wallace, F. H. Richter, J. H. J. Thijssen, P. G. Bruce, *Energy Environ. Sci.* **2018**, *11*, 185–201.
- [46] W. Yang, J. Yang, J. J. Byun, F. P. Moissinac, J. Xu, S. J. Haigh, M. Domingos, M. A. Bissett, R. A. Dryfe, S. Barg, *Adv. Mater.* **2019**, *31*, 1902725.
- [47] C. Sun, S. Liu, X. Shi, C. Lai, J. Liang, Y. Chen, *Chem. Eng. J.* **2020**, *381*, 122641.
- [48] C. Zhang, K. Shen, B. Li, S. Li, S. Yang, *J. Mater. Chem. A* **2018**, *6*, 19960–19966.
- [49] J. Zhao, Y. Zhang, Y. Huang, J. Xie, X. Zhao, C. Li, J. Qu, Q. Zhang, J. Sun, B. He, Q. Li, C. Lu, X. Xu, W. Lu, L. Li, Y. Yao, *Adv. Sci.* **2018**, *5*, 1801114.
- [50] F. Zhang, M. Wei, V. V. Viswanathan, B. Swart, Y. Shao, G. Wu, C. Zhou, *Nano Energy* **2017**, *40*, 418–431.
- [51] K. Fu, Y. Yao, J. Dai, L. Hu, *Adv. Mater.* **2017**, 29.
- [52] C. Zhu, T. Liu, F. Qian, W. Chen, S. Chandrasekaran, B. Yao, Y. Song, E. B. Duoss, J. D. Kuntz, C. M. Spadaccini, M. A. Worsley, Y. Li, *Nano Today* **2017**.
- [53] P. Chang, H. Mei, S. Zhou, K. G. Dassios, L. Cheng, *J. Mater. Chem. A* **2019**.
- [54] A. Active Standard, West Conshohocken: ASTM Int **2012**.
- [55] J. Huang, J. Yang, W. Li, W. Cai, Z. Jiang, *Thin Solid Films* **2008**, *516*, 3314–3319.
- [56] P. Chen, H. Chen, J. Qiu, C. Zhou, *Nano Res.* **2010**, *3*, 594–603.
- [57] F. Xu, T. Wang, W. Li, Z. Jiang, *Chem. Phys. Lett.* **2003**, *375*, 247–251.
- [58] A. Azhari, E. Marzbanrad, D. Yilmaz, E. Toyserkani, M. A. Pope, *Carbon* **2017**, *119*, 257–266.
- [59] J. A. Lewis, *Adv. Funct. Mater.* **2006**, *16*, 2193–2204.
- [60] E. B. Duoss, M. Twardowski, J. A. Lewis, *Adv. Mater.* **2007**, *19*, 3485–3489.
- [61] K. Fu, Y. B. Wang, C. Y. Yan, Y. G. Yao, Y. A. Chen, J. Q. Dai, S. Lacey, J. Y. Wan, T. Li, Z. Y. Wang, Y. Xu, L. B. Hu, *Adv. Mater.* **2016**, *28*, 2587–2594.
- [62] K. Shen, J. Ding, S. Yang, *Adv. Energy Mater.* **2018**, *8*, 1800408.
- [63] J. Hu, Y. Jiang, S. Cui, Y. Duan, T. Liu, H. Guo, L. Lin, Y. Lin, J. Zheng, K. Amine, *Adv. Energy Mater.* **2016**, *6*, 1600856.
- [64] A. J. Blake, R. R. Kohlmeyer, J. O. Hardin, E. A. Carmona, B. Maruyama, J. D. Berrigan, H. Huang, M. F. Durstock, *Adv. Energy Mater.* **2017**, *7*, 1602920.
- [65] M. Cheng, Y. Jiang, W. Yao, Y. Yuan, R. Deivanayagam, T. Foroozan, Z. Huang, B. Song, R. Rojaee, T. Shokuhfar, Y. Pan, J. Lu, R. Shahbazian-Yassar, *Adv. Mater.* **2018**, *30*, e1800615.
- [66] J. A. Lewis, J. E. Smay, J. Stuecker, J. Cesarano, *J. Am. Ceram. Soc.* **2006**, *89*, 3599–3609.
- [67] J. A. Lewis, G. M. Gratson, *Mater. Today* **2004**, *7*, 32–39.
- [68] J. E. Smay, J. Cesarano, J. A. Lewis, *Langmuir* **2002**, *18*, 5429–5437.
- [69] J. E. Smay, G. M. Gratson, R. F. Shepherd, J. Cesarano, J. A. Lewis, *Adv. Mater.* **2002**, *14*, 1279–1283.
- [70] N. Mostafa, H. M. Syed, S. Igor, G. Andrew, *Tsinghua Sci. Technol.* **2009**, *14*, 29–37.
- [71] S. Masood, W. Song, *Mater. Des.* **2004**, *25*, 587–594.
- [72] C. W. Foster, M. P. Down, Y. Zhang, X. Ji, S. J. Rowley-Neale, G. C. Smith, P. J. Kelly, C. E. Banks, *Sci. Rep.* **2017**, *7*, 42233.
- [73] A. Maurel, M. Courty, B. Fleutot, H. Tortajada, K. Prashantha, M. Armand, S. Grangeon, S. Panier, L. Dupont, *Chem. Mater.* **2018**, *30*, 7484–7493.
- [74] C. Reyes, R. Somogyi, S. Niu, M. A. Cruz, F. Yang, M. J. Catenacci, C. P. Rhodes, B. J. Wiley, *ACS Appl. Energy Mater.* **2018**, *1*, 5268–5279.
- [75] O. A. Mohamed, S. H. Masood, J. L. Bhowmik, *Adv. Manuf.* **2015**, *3*, 42–53.
- [76] J. Wang, A. Goyanes, S. Gaisford, A. W. Basit, *Int. J. Pharm.* **2016**, *503*, 207–212.
- [77] F. P. Melchels, J. Feijen, D. W. Grijpma, *Biomaterials* **2010**, *31*, 6121–6130.
- [78] Q. Chen, R. Xu, Z. He, K. Zhao, L. Pan, *J. Electrochem. Soc.* **2017**, *164*, A1852–A1857.
- [79] R. M. Hensleigh, H. Cui, J. S. Oakdale, J. C. Ye, P. G. Campbell, E. B. Duoss, C. M. Spadaccini, X. Zheng, M. A. Worsley, *Mater. Horiz.* **2018**, *5*, 1035–1041.
- [80] Q. Zhang, F. Zhang, X. Xu, C. Zhou, D. Lin, *ACS Nano* **2018**, *12*, 1096–1106.
- [81] J.-P. Kruth, X. Wang, T. Laoui, L. Froyen, *Assembly Automation* **2003**, *23*, 357–371.
- [82] J. Sha, Y. Li, R. Villegas Salvatierra, T. Wang, P. Dong, Y. Ji, S. K. Lee, C. Zhang, J. Zhang, R. H. Smith, P. M. Ajayan, J. Lou, N. Zhao, J. M. Tour, *ACS Nano* **2017**, *11*, 6860–6867.
- [83] J. Bauer, A. Schroer, R. Schwaiger, O. Kraft, *Nat. Mater.* **2016**, *15*, 438–443.
- [84] A. Tanwilaisiri, Y. Xu, R. Zhang, D. Harrison, J. Fyson, M. Areir, *J. Energy Storage* **2018**, *16*, 1–7.
- [85] P. Shah, R. Racasan, P. Bills, *Case studies in nondestructive testing and evaluation* **2016**, *6*, 69–78.
- [86] P. Jiang, Z. Ji, X. Zhang, Z. Liu, X. Wang, *Progress in Additive Manufacturing* **2017**, *3*, 65–86.
- [87] J. T. Sutton, K. Rajan, D. P. Harper, S. C. Chmely, *ACS Appl. Mater. Interfaces* **2018**, *10*, 36456–36463.
- [88] S. C. Ligon, R. Liska, J. r. Stampfl, M. Gurr, R. Mülhaupt, *Chem. Rev.* **2017**, *117*, 10212–10290.
- [89] S. H. Park, M. Kaur, D. Yun, W. S. Kim, *Langmuir* **2018**, *34*, 10897–10904.
- [90] T.-S. Wei, B. Y. Ahn, J. Grotto, J. A. Lewis, *Adv. Mater.* **2018**, *30*, 1703027.
- [91] A. E. Jakus, E. B. Secor, A. L. Rutz, S. W. Jordan, M. C. Hersam, R. N. Shah, *ACS Nano* **2015**, *9*, 4636–4648.
- [92] T. Gao, Z. Yang, C. Chen, Y. Li, K. Fu, J. Dai, E. M. Hitz, H. Xie, B. Liu, J. Song, B. Yang, L. Hu, *ACS Nano* **2017**, *11*, 11513–11520.
- [93] S. S. Zhang, *J. Power Sources* **2007**, *164*, 351–364.
- [94] Z. Xue, D. He, X. Xie, *J. Mater. Chem. A* **2015**, *3*, 19218–19253.
- [95] V. Thangadurai, S. Narayanan, D. Pinzarlu, *Chem. Soc. Rev.* **2014**, *43*, 4714–4727.
- [96] J. C. Bachman, S. Muy, A. Grimaud, H.-H. Chang, N. Pour, S. F. Lux, O. Paschos, F. Maglia, S. Lupart, P. Lamp, *Chem. Rev.* **2015**, *116*, 140–162.
- [97] D. W. McOwen, S. Xu, Y. Gong, Y. Wen, G. L. Godbey, J. E. Gritton, T. R. Hamann, J. Dai, G. T. Hitz, L. Hu, E. D. Wachsman, *Adv. Mater.* **2018**, *30*, e1707132.
- [98] J.-K. Kim, Y. J. Lim, H. Kim, G.-B. Cho, Y. Kim, *Energy Environ. Sci.* **2015**, *8*, 3589–3596.
- [99] J. Liu, Z. Xu, X. Li, Y. Zhang, Y. Zhou, Z. Wang, X. Wang, *Sep. Purif. Technol.* **2007**, *58*, 53–60.
- [100] S. Xin, Y. You, S. Wang, H.-C. Gao, Y.-X. Yin, Y.-G. Guo, *ACS Energy Lett.* **2017**, *2*, 1385–1394.
- [101] H. Duan, Y. X. Yin, Y. Shi, P. F. Wang, X. D. Zhang, C. P. Yang, J. L. Shi, R. Wen, Y. G. Guo, L. J. Wan, *J. Am. Chem. Soc.* **2018**, *140*, 82–85.
- [102] E. Frackowiak, *Phys. Chem. Chem. Phys.* **2007**, *9*, 1774–1785.
- [103] L. L. Zhang, X. Zhao, *Chem. Soc. Rev.* **2009**, *38*, 2520–2531.
- [104] E. Frackowiak, F. Beguin, *Carbon* **2001**, *39*, 937–950.
- [105] J. H. Kim, W. S. Chang, D. Kim, J. R. Yang, J. T. Han, G. W. Lee, J. T. Kim, S. K. Seol, *Adv. Mater.* **2015**, *27*, 157–161.
- [106] J. H. Kim, S. Lee, M. Wahajat, H. Jeong, W. S. Chang, H. J. Jeong, J. R. Yang, J. T. Kim, S. K. Seol, *ACS Nano* **2016**, *10*, 8879–8887.
- [107] A. Azhari, E. Toyserkani, C. Villain, *Int. J. Appl. Ceram. Technol.* **2015**, *12*, 8–17.
- [108] T. Wang, L. Li, X. Tian, H. Jin, K. Tang, S. Hou, H. Zhou, X. Yu, *Electrochim. Acta* **2019**, *319*, 245–252.
- [109] X. Tian, K. Tang, H. Jin, T. Wang, X. Liu, W. Yang, Z. Zou, S. Hou, K. Zhou, *Carbon* **2019**, *155*, 562–569.
- [110] M. Islam, E. Rojas, D. Bergey, A. Johnson, A. Yodh, *Nano Lett.* **2003**, *3*, 269–273.
- [111] B. Chen, Y. Jiang, X. Tang, Y. Pan, S. Hu, *ACS Appl. Mater. Interfaces* **2017**, *9*, 28433–28440.

- [112] L. Li, J. Zhang, Z. Peng, Y. Li, C. Gao, Y. Ji, R. Ye, N. D. Kim, Q. Zhong, Y. Yang, H. Fei, G. Ruan, J. M. Tour, *Adv. Mater.* **2016**, *28*, 838–845.
- [113] C. Zhao, C. Wang, R. Gorkin, S. Beirne, K. Shu, G. G. Wallace, *Electrochem. Commun.* **2014**, *41*, 20–23.
- [114] S. Hashmi, R. Latham, R. Linford, W. Schlindwein, *Polym. Int.* **1998**, *47*, 28–33.
- [115] M. Beidaghi, C. Wang, *Electrochim. Acta* **2011**, *56*, 9508–9514.
- [116] W. Li, Y. Zhou, I. R. Howell, Y. Gai, A. R. Naik, S. Li, K. R. Carter, J. J. Watkins, *ACS Appl. Mater. Interfaces* **2018**, *10*, 5447–5454.
- [117] Z. Du, K. Rollag, J. Li, S. An, M. Wood, Y. Sheng, P. Mukherjee, C. Daniel, D. Wood, *J. Power Sources* **2017**, *354*, 200–206.
- [118] J. Christensen, P. Albertus, R. S. Sanchez-Carrera, T. Lohmann, B. Kozinsky, R. Liedtke, J. Ahmed, A. Kojic, *J. Electrochem. Soc.* **2011**, *159*, R1-R30.
- [119] Z. Ma, X. Yuan, L. Li, Z.-F. Ma, D. P. Wilkinson, L. Zhang, J. Zhang, *Energy Environ. Sci.* **2015**, *8*, 2144–2198.
- [120] X. Zhang, C. Wang, H. Li, X.-G. Wang, Y.-N. Chen, Z. Xie, Z. Zhou, *J. Mater. Chem. A* **2018**, *6*, 2792–2796.
- [121] Z. Zhang, X. G. Wang, X. Zhang, Z. Xie, Y. N. Chen, L. Ma, Z. Peng, Z. Zhou, *Adv. Sci.* **2018**, *5*, 1700567.
- [122] C. Zhu, T. Y. Han, E. B. Duoss, A. M. Golobic, J. D. Kuntz, C. M. Spadaccini, M. A. Worsley, *Nat. Commun.* **2015**, *6*, 6962.
- [123] Q. Zhang, F. Zhang, S. P. Medarametla, H. Li, C. Zhou, D. Lin, *Small* **2016**, *12*, 1702–1708.
- [124] C. Zhu, T. Liu, F. Qian, T. Y. Han, E. B. Duoss, J. D. Kuntz, C. M. Spadaccini, M. A. Worsley, Y. Li, *Nano Lett.* **2016**, *16*, 3448–3456.
- [125] B. Yao, S. Chandrasekaran, J. Zhang, W. Xiao, F. Qian, C. Zhu, E. B. Duoss, C. M. Spadaccini, M. A. Worsley, Y. Li, *Joule* **2019**, *3*, 459–470.
- [126] X. Tang, H. Zhou, Z. Cai, D. Cheng, P. He, P. Xie, D. Zhang, T. Fan, *ACS Nano* **2018**, *12*, 3502–3511.
- [127] X. Cai, M. Peng, X. Yu, Y. Fu, D. Zou, *J. Mater. Chem. C* **2014**, *2*, 1184–1200.
- [128] J. Liu, K. Song, P. A. van Aken, J. Maier, Y. Yu, *Nano Lett.* **2014**, *14*, 2597–2603.
- [129] W. Liu, Z. Chen, G. Zhou, Y. Sun, H. R. Lee, C. Liu, H. Yao, Z. Bao, Y. Cui, *Adv. Mater.* **2016**, *28*, 3578–3583.
- [130] Y. Liu, Y. Qiao, Y. Zhang, Z. Yang, T. Gao, D. Kirsch, B. Liu, J. Song, B. Yang, L. Hu, *Energy Storage Mater.* **2018**, *12*, 197–203.
- [131] P. Xu, B. Wei, Z. Cao, J. Zheng, K. Gong, F. Li, J. Yu, Q. Li, W. Lu, J.-H. Byun, *ACS Nano* **2015**, *9*, 6088–6096.
- [132] L. Kou, T. Huang, B. Zheng, Y. Han, X. Zhao, K. Gopalsamy, H. Sun, C. Gao, *Nat. Commun.* **2014**, *5*, 3754.
- [133] Z. Dong, C. Jiang, H. Cheng, Y. Zhao, G. Shi, L. Jiang, L. Qu, *Adv. Mater.* **2012**, *24*, 1856–1861.
- [134] R. Wang, J. Lang, P. Zhang, Z. Lin, X. Yan, *Adv. Funct. Mater.* **2015**, *25*, 2270–2278.
- [135] Z. Wang, Q. e. Zhang, S. Long, Y. Luo, P. Yu, Z. Tan, J. Bai, B. Qu, Y. Yang, J. Shi, *ACS Appl. Mater. Interfaces* **2018**, *10*, 10437–10444.
- [136] C. Zhang, M. P. Kremer, A. Seral-Ascaso, S. H. Park, N. McEvoy, B. Anasori, Y. Gogotsi, V. Nicolosi, *Adv. Funct. Mater.* **2018**, *28*, 1705506.
- [137] S. Wang, Y. Yu, R. Li, G. Feng, Z. Wu, G. Compagnini, A. Gulino, Z. Feng, A. Hu, *Electrochim. Acta* **2017**, *241*, 153–161.

Manuscript received: September 23, 2019

Revised manuscript received: December 8, 2019

Accepted manuscript online: December 9, 2019

Version of record online: January 9, 2020